Howard Hughes Medical Institute

Published as: *Cell*. 2021 October 14; 184(21): 5375–5390.e16.

Structural basis and regulation of the reductive stress response

Andrew G. Manford[1,2,*], **Elijah L. Mena**[1,2,6,*], **Karen Y. Shih**[1,2], **Christine L. Gee**[1,2], **Rachael McMinimy**[1], **Brenda Martínez-González**[1], **Rumi Sherriff**[1], **Brandon Lew**[1,2], **Madeline Zoltek**[1], **Fernando Rodríguez-Pérez**[1], **Makda Woldesenbet**[1], **John Kuriyan**[1,2,3,4,5], **Michael Rape**[1,2,3,#,@]

[1]Department of Molecular and Cell Biology, University of California at Berkeley, Berkeley CA 94720, USA

[2]Howard Hughes Medical Institute, University of California at Berkeley, Berkeley CA 94720, USA

[3]California Institute for Quantitative Biosciences (QB3), University of California at Berkeley, Berkeley, CA 94720, USA

[4]Molecular Biophysics and Integrative Bio-Imaging Division, Lawrence Berkeley National Laboratory, Berkeley, CA 94720, USA

[5]Department of Chemistry, University of California at Berkeley, Berkeley CA 94720, USA

[6]current address: Department of Genetics, Harvard Medical School, Boston, MA 02115

Abstract

While oxidative phosphorylation is best known for producing ATP, it also yields reactive oxygen species (ROS) as invariant byproducts. Depletion of ROS below their physiological levels, or reductive stress, impedes cellular signaling and has been linked to cancer, diabetes, and cardiomyopathy. Cells alleviate reductive stress by ubiquitylating and degrading the mitochondrial gatekeeper FNIP1, yet how the responsible E3 ligase $CUL2^{FEM1B}$ can bind its target based on redox state and how this is adjusted to changing cellular environments is unknown. Here, we show that $CUL2^{FEM1B}$ relies on zinc as a molecular glue to selectively recruit reduced FNIP1 during

[#]to whom correspondence should be addressed: mrape@berkeley.edu.
[*]these authors contributed equally
[@]lead author: mrape@berkeley.edu

Author contributions

Conceptualization: A.G.M., E.L.M., J.K., M.R.; Methodology: A.G.M., E.L.M., C.L.G., J.K., M.R.; Investigation: A.G.M., E.L.M., K.Y.S., C.L.G., R.M., B.M.G., R.S., B.L., M.Z., F.R.P., M.W.; Writing – original draft: A.G.M., E.L.M., C.L.G., M.R.; Writing – review and editing: A.G.M., E.L.M., C.L.G., J.K., M.R.; Funding Acquisition: J.K., M.R.; Resources: J.K., M.R.; Supervision: A.G.M., J.K., M.R.

Declaration of Interests

MR and JK are co-founders and members of the SAB of Nurix Tx. MR is on the SAB of Monte Rosa Tx and an iPartner at The Column Group. JK is on the SAB of Revolution Medicine and Carmot Tx.

Inclusion and Diversity

One or more of the authors of this paper self-identifies as an underrepresented ethnic minority in science. One or more of the authors of this paper received support from a program designed to increase minority representation in science. One or more of the authors of this paper self-identifies as a member of the LGBTQ+ community.

reductive stress. FNIP1 ubiquitylation is gated by pseudosubstrate inhibitors of the BEX family, which prevent premature FNIP1 degradation to protect cells from unwarranted ROS accumulation. *FEM1B* gain-of-function mutation and *BEX* deletion elicit similar developmental syndromes, showing that the zinc-dependent reductive stress response must be tightly regulated to maintain cellular and organismal homeostasis.

Graphical Abstract

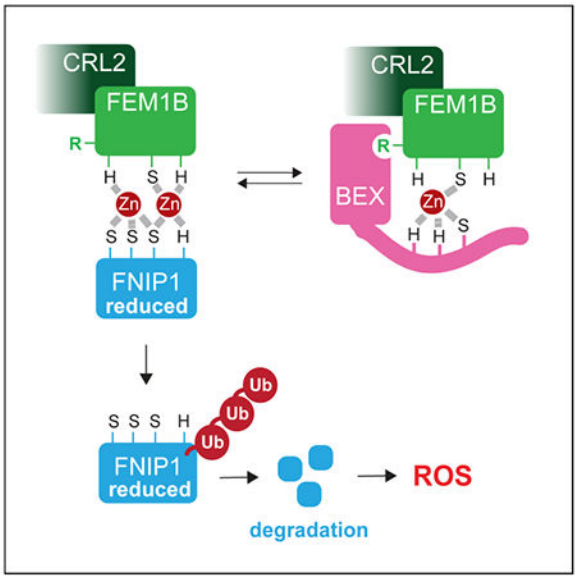

eTOC

Different from protein interactions mediated by amino acid side chains, the E3 ligase $CUL2^{FEM1B}$ selectively recruits the reduced FNIP1 that emerges upon reductive stress through zinc ions at the interface of E3 ligase and substrate. This interaction is gated by pseudosubstrate inhibitors of the BEX family.

Keywords

ubiquitin; CUL2; FEM1B; reductive stress; mitochondria; oxidative phosphorylation

Introduction

Mitochondria possess crucial roles in metabolism and signaling that ensure tissue formation and homeostasis (Chandel, 2015; Spinelli and Haigis, 2018; Tan and Finkel, 2020). Central among their many functions is oxidative phosphorylation, which produces ATP to sustain a cell's energy balance (Lisowski et al., 2018). As ATP requirements can change, cells must constantly adjust oxidative phosphorylation to their needs, as illustrated by differentiating cells that activate mitochondrial ATP synthesis to fulfill the escalating energy demands of cell fate specification (Beckervordersandforth et al., 2017). Dysregulation of oxidative phosphorylation accordingly impedes development (Gorman et al., 2016), yet how this

process is tuned to the necessities of tissue formation and homeostasis is still incompletely understood.

In addition to ATP, oxidative phosphorylation yields reactive oxygen species (ROS) as invariant byproducts. Mutations in components of the electron transport chain, abrupt changes in the rate of oxidative phosphorylation, or environmental toxins can increase ROS to levels that damage proteins, lipids, or DNA (Sies et al., 2017). If unmitigated, such oxidative stress exhausts stem cell populations, accelerates aging, and results in cancer or neurodegeneration (Corenblum et al., 2016; Ito et al., 2004; Papa et al., 2019; Suda et al., 2011). Cells sense oxidative stress through the E3 ligase $CUL3^{KEAP1}$, which is inhibited by ROS-dependent oxidation of Cys residues in KEAP1 (Dinkova-Kostova et al., 2002; Itoh et al., 1999; Itoh et al., 2003; Zhang et al., 2004; Zipper and Mulcahy, 2002). Inhibition of $CUL3^{KEAP1}$ prevents the degradation of the transcription factor NRF2 and thereby instigates an antioxidant gene expression program.

While overabundant ROS elicit oxidative stress, their persistent depletion leads to the opposite condition known as reductive stress (Gores et al., 1989; Manford et al., 2020; Tan and Finkel, 2020). Reductive stress can be caused by inactive oxidative phosphorylation or prolonged antioxidant signaling (Best and Sutherland, 2018; Manford et al., 2020; Rajasekaran et al., 2007; Rajasekaran et al., 2011) and if unopposed, blocks cell differentiation (Manford et al., 2020; Rajasekaran et al., 2020) or results in cancer, diabetes, or cardiomyopathy (Bellezza et al., 2018). Cells detect reductive stress through the FNIP1 protein, which contains three conserved Cys residues that are selectively reduced upon ROS depletion (Manford et al., 2020). The E3 ligase $CUL2^{FEM1B}$ ubiquitylates reduced FNIP1 to trigger its proteasomal degradation, which allows cells to re-activate oxidative phosphorylation and replenish their ROS supply. Key to the reductive stress response is the ability of $CUL2^{FEM1B}$ to distinguish reduced from oxidized FNIP1 (Manford et al., 2020), but how an E3 ligase can discriminate targets based on redox state remains unknown.

Underscoring the importance of the reductive stress response, mutations in its core components impede development and cause disease. Loss of *FNIP1* inhibits B cell differentiation and causes agammaglobulinemia and hypertrophic cardiomyopathy (Baba et al., 2012; Saettini et al., 2020), while heterozygous mutation of the R126 residue in FEM1B results in syndromic global developmental delay with intellectual disability (Lecoquierre et al., 2019). As deletion of a single *FEM1B* allele in mice did not reveal phenotypes (Lu et al., 2005), mutation of R126 likely exerts a gain of function that disrupts development. This suggested that reductive stress signaling must be strictly controlled, yet regulators of this pathway have not been identified.

Here, we report the structural basis and regulation of the reductive stress response. Using X-ray crystallography, we found that $CUL2^{FEM1B}$ relies on zinc to selectively bind reduced, but not oxidized, FNIP1. Zinc functions in analogy to molecular glues that elicit protein degradation in a therapeutic setting (Jevtic et al., 2021; Petzold et al., 2016; Simonetta et al., 2019). Although the critical residue in disease, R126, is located within the substrate binding pocket of FEM1B, it does not engage FNIP1 but recruits BEX proteins as pseudosubstrate inhibitors of $CUL2^{FEM1B}$. Loss of *BEX* genes in patients with Xq22 deletion and mutation

of R126 in *FEM1B* cause similar developmental syndromes (Hijazi et al., 2020; Lecoquierre et al., 2019), showing that regulation of the reductive stress response plays a crucial role in ensuring tissue formation.

Results

Zinc-dependent recognition of reduced FNIP1

Reductive stress signaling relies on the selective recognition of reduced FNIP1 by $CUL2^{FEM1B}$ (Manford et al., 2020). To reveal the molecular basis of this signaling circuit, we identified a FEM1B construct with six annotated ankyrin repeats and one TPR repeat that was sufficient to capture the FNIP1 degron (Figure S1A). We purified the complex between this FEM1B construct and a 30-residue FNIP1 degron to homogeneity (Figure S1B) and determined its X-ray crystal structure to a resolution of 2.9 Å (Figure 1A; Figure S1C–G; Table S1).

Consistent with recent work (Chen et al., 2021), the ankyrin repeats of FEM1B combined with an amino-terminal ankyrin-like repeat to form a crescent-shaped molecule that is capped on its carboxy terminus by helix-turn-helix and TPR motifs (Figure 1B). Of the four FEM1B molecules in the asymmetric unit, two showed clear density for a bound degron (Figure S1D, E; Figure S2A). The structures of all FEM1B molecules in the asymmetric unit were highly similar to each other (Figure S2A), and FEM1B adopted the same conformation without substrate or when in complex with a distinct target, a C-end rule degron (Chen et al., 2021). These findings suggested that substrate binding does not elicit major conformational changes in FEM1B.

FEM1B engages FNIP1 in a deep groove on its concave side (Figure 1A), which places the substrate close to residues of both the ankyrin repeats and TPR motif. FEM1B binds its critical target, FNIP1, through a surface that is similar to several other ankyrin-repeat proteins (DaRosa et al., 2018; Nam et al., 2006; Pan et al., 2018; Verardi et al., 2017; Wilson and Kovall, 2006) (Figure S2B), but distinct from the ankyrin-repeat E3 ligase $CUL5^{ASB9}$ (Lumpkin et al., 2020) (Figure S2C). To gain access to its binding pocket on FEM1B, FNIP1 forms an extended loop that is characterized by a sharp turn imposed by a Pro residue (Figure 1A, B). This loop orients the three conserved Cys residues of the FNIP1 degron towards FEM1B. Although the FNIP1 loop docks onto a similar region of FEM1B as the C-end rule degron, it does not engage FEM1B residues critical for C-end rule recognition (Figure S2D).

Despite its similarities with other ankyrin-repeat proteins, $CUL2^{FEM1B}$ uses a distinct mechanism to recognize its substrate. Most proteins rely on interactions between amino acid side chains or the peptide backbone to engage their targets. In stark contrast, the complex between FEM1B and FNIP1 is predominantly mediated by two Zn^{2+} ions coordinated at the interface between FEM1B and the tip of the FNIP1 degron loop (Figure 1A; Figure S1F, G). We detected Zn^{2+} in FEM1B-FNIP1 complexes by X-ray diffraction (Figure S3A), X-ray fluorescence (Figure S3B), and inductively coupled plasma spectroscopy (Figure S3C). When we removed zinc by N,N,N’,N’-tetrakis(2-pyridinylmethyl)-1,2-ethanediamine (TPEN), binding of FNIP1 to recombinant FEM1B was lost in a dose-dependent manner

(Figure 1C, D), while increasing Zn^{2+} levels allowed FEM1B to bind more FNIP1 (Figure 1D). Only Zn^{2+}, but not several other metal ions, was able to stabilize the FEM1B-FNIP1 interaction (Figure S3D).

Consistent with these biochemical data, reducing cellular zinc levels with TPEN prevented substrate binding by FEM1B without disrupting the integrity of $CUL2^{FEM1B}$ (Figure 1E). A flow cytometry assay, which measures the abundance of GFP fused to the FNIP1 degron (GFP^{degron}) (Manford et al., 2020), accordingly revealed that TPEN protected FNIP1 from FEM1B-induced degradation (Figure 1F). The same treatment did not affect a reporter that is turned over through $CUL4^{CRBN}$ (Figure S3E, although this E3 ligase shares the RING subunit RBX1 with $CUL2^{FEM1B}$ (Fischer et al., 2014). At our concentrations, TPEN therefore strongly inhibited substrate binding by $CUL2^{FEM1B}$, yet it did not extract zinc from the RING domain. We conclude that interface zinc ions play an essential role in mediating FNIP1 recognition by $CUL2^{FEM1B}$.

A Cys/His claw coordinates zinc at the protein interface

Most proteins bind zinc through Cys or His residues (Kocyla et al., 2021). In line with this notion, the zinc ions at the interface between FEM1B and FNIP1 are coordinated by one Cys (C186) and two His residues (H185, H218) of FEM1B and three Cys residues (C580; C582; C585) and one histidine (H587) of FNIP1 (Figure 2A, B). Compared to its apo-structure (Chen et al., 2021), both His residues of FEM1B rotate towards the metal ions in the FEM1B-FNIP1 complex (Figure S4A). This results in a C3H1 motif to coordinate one zinc, while the adjacent ion is chelated by a C2H2 motif.

Mutation of FNIP1-C580, C582, or H587, which engage one zinc, impaired detection of the FNIP1 degron by FEM1B, while mutation of FNIP1-C585, which is located between both zinc ions, abrogated FNIP1 recognition (Figure 2C). Simultaneous mutation of C580 and C582, which bind one zinc each, also blocked capture of FNIP1 by recombinant FEM1B. In a similar manner, C186 of FEM1B was essential for FNIP1 recognition *in vitro* (Figure 2D). As expected from these experiments, mutation of the Zn^{2+}-coordinating Cys residues of FNIP1 strongly impaired substrate ubiquitylation by recombinant NEDD8-modified $CUL2^{FEM1B}$ (Figure 2E).

In cells, all Zn^{2+}-binding residues in FEM1B were required for recognition of endogenous FNIP1 (Figure 2F). We had previously found that mutation of C580, C582 or H587 in FNIP1 also obliterated its binding to FEM1B in cells (Manford et al., 2020); as mutation of these residues only impeded degron recognition *in vitro* (Figure 2C), reduced flexibility of full-length FNIP1 bound to FLCN might impose even stricter Zn^{2+} dependency on substrate recognition by $CUL2^{FEM1B}$. In line with these binding studies, mutation of C186 in FEM1B blocked turnover of the GFP^{degron} reporter (Figure 2G), and all Zn^{2+}-binding residues of FEM1B were required for efficient degradation of a sensitized reporter built around the FNIP1-C582S degron (Figure 2H). By contrast, mutation of FEM1B residues involved in detection of the C-end rule substrate did not inhibit GFP^{degron} turnover (Figure S4B), and conversely, C186 of FEM1B was not required for degradation of a C-end rule reporter (Figure S4C). We conclude that Zn^{2+} acts in analogy to molecular glues to recruit $CUL2^{FEM1B}$ to its reductive stress substrate, FNIP1. As only reduced, but not oxidized, Cys

residues can chelate Zn^{2+} (Evans et al., 2002; Schmalen et al., 2014), these findings provide an explanation for the redox-sensitive detection of FNIP1 by $CUL2^{FEM1B}$.

A Lys/Tyr finger orients the FNIP1 degron

Despite the strict conservation of its degron Cys residues, a FNIP1 reporter with its essential C585 moved by five positions was still degraded through $CUL2^{FEM1B}$ (Figure S4D). This indicated that FEM1B can recognize multiple conformations adopted by a flexible degron loop. As cells express many proteins with Cys- and His-rich regions, we hypothesized that additional features of the FEM1B-FNIP1 interface contribute to the specificity of this interaction. Indeed, our structure revealed that a conserved Tyr residue, Y584, docks into a FEM1B pocket that is adjacent to the zinc interface (Figure 3A, B). Y584 of FNIP1 as well as an upstream Lys residue, K583, form interactions with FEM1B Ile341, Met220, Glu228, Ser229, and the peptide bond oxygen of Val225.

Mutation of K583 and Y584 of FNIP1 impaired, but did not block, recognition of the degron by FEM1B *in vitro* (Figure 3C), while these variants showed strongly reduced ubiquitylation by recombinant $CUL2^{FEM1B}$ (Figure 3D). The degron residues K583 and Y584, which we refer to as the KY-finger, are therefore important, yet not essential, for FNIP1 recognition by FEM1B. In line with this notion, K583 or Y584 were required for the $CUL2^{FEM1B}$-dependent degradation of the sensitized FNIP1-C582S degron reporter (Figure 3E), although an otherwise wildtype GFP^{degron} was turned over in the presence of these mutations (Figure S4E). Similar observations were made for the respective residues of FEM1B: mutation of Glu196, Met220, Val225, and Glu228 abolished FEM1B-dependent degradation of FNIP1-C582S, but not the wildtype GFP^{degron}, reporter (Figure 3F; Figure S4F). From these results, we infer that the KY-finger of FNIP1 docks into a FEM1B pocket and likely orients the degron on the E3 surface for efficient ubiquitylation.

Disease mutation activates FEM1B

Given the conservation of FEM1B's substrate binding pocket (Figure 4A), we were surprised to see that FNIP1 only occupies part of this surface. Instead of contacting FNIP1, FEM1B residues in the remaining pocket coordinate a buffer HEPES molecule (Figure 4A–C). FEM1B R126, whose mutation causes syndromic developmental delay (Lecoquierre et al., 2019), bound the charged HEPES sulfonate group (Figure 4B, C). The neighboring S122 of FEM1B formed an additional hydrogen bond to the sulfonate group of HEPES (Figure 4C), while the remainder of this molecule was tucked into a pocket established by several hydrophobic and aromatic residues of FEM1B.

As expected from its limited interactions with FNIP1, mutation of R126 did not prevent binding of recombinant FEM1B to the FNIP1 degron (Figure 4D), and $FEM1B^{R126A}$ ubiquitylated FNIP1 with similar efficiency as FEM1B (Figure 4E). Replacing HEPES with Tris, which cannot be bound by R126, also did not impact the affinity of FEM1B to the FNIP1 degron (Figure S5A). In striking contrast, $FEM1B^{R126Q}$ and $FEM1B^{R126A}$ bound FNIP1-FLCN much better than wildtype FEM1B in cells (Figure 4F), and both variants triggered degradation of the FNIP1 reporter much more efficiently than their wildtype counterpart (Figure 4G). These effects were specific for FNIP1, as FEM1B and

FEM1B^{R126A} targeted a C-end rule degron reporter with similar efficiency (Figure S5B). Consistent with the heterozygous *FEM1B* mutation in disease (Lecoquierre et al., 2019), loss of R126 therefore results in a gain of function towards FNIP1 in cells, even though it did not impact recognition in purified settings.

Human BEX proteins bind FEM1B dependent on R126

We hypothesized that an inhibitory factor, which is absent from reconstituted systems but can engage FEM1B in cells, accounts for the discrepancy between the *in vitro* and *in vivo* phenotypes of R126 mutations. We thus used affinity purification and mass spectrometry to search for proteins bound by FEM1B, but not FEM1B^{R126A}. In these experiments, we also mutated L597 of FEM1B, which inhibits integration of FEM1B into the CUL2 module and allowed us to monitor FEM1B substrates (Manford et al., 2020). In line with our previous results, FEM1B$^{R126A/L597A}$ bound FNIP1 and its partner FLCN more efficiently than FEM1B^{L597A} (Figure 5A). As this increased interaction of FNIP1 was lost upon concomitant mutation of FEM1B-C186, FEM1B^{R126} variants recognize FNIP1 through the canonical substrate binding site (Figure S6A). These observations supported the notion that R126 of FEM1B is critical for recruiting an inhibitor of reductive stress signaling.

Pointing towards this potential inhibitor, FEM1B^{R126} variants failed to bind all five BEX proteins (Figure 5A). The BEX proteins are encoded by a eutherian-specific gene cluster, whose products have been ascribed a wide range of functions in cell proliferation and survival (Navas-Perez et al., 2020). Most intriguingly, *BEX* genes are lost in patients of Xq22 deletion syndrome, a developmental delay and intellectual disability syndrome that is similar to that caused by R126 mutation in *FEM1B* (Hijazi et al., 2020). Using affinity purification and Western blotting, we confirmed that FEM1B bound multiple BEX proteins dependent upon R126 of FEM1B (Figure 5B, C; Figure S6B). Endogenous FEM1B associated particularly well with BEX2 and BEX3, which occupied ~60% of FEM1B molecules in 293T cells (Figure 5D; Figure S6C). As BEX2 recognized FEM1B *in vitro*, the BEX proteins and FEM1B directly engage each other (Figure S6D).

The BEX proteins did not bind the FEM1B homolog, FEM1A (Figure S6E), which lacks zinc-chelating residues (Chen et al., 2021; Koren et al., 2018). Conversely, mutation of C186 in FEM1B impaired recognition of BEX2 or BEX3 (Figure 5C; Figure S6B). Mutation of a Cys in BEX3, or deletion of 15 carboxy-terminal residues that contain this Cys as well as a cluster of His residues, impaired the interaction of BEX3 with FEM1B (Figure 5E; Figure S6F), and zinc chelation with 1,10-phenanthroline blocked the remaining interaction of BEX2 with FEM1B^{R126A} *in vitro* (Figure S6D). This suggested that the BEX proteins might not only engage R126 of FEM1B, but also the Zn^{2+}-dependent part of the substrate binding pocket.

To directly test for a role of Zn^{2+} in complex formation, we synthesized a TAMRA-labeled peptide of the BEX3 carboxy-terminus (CTP) and monitored its recognition by FEM1B using fluorescence polarization. FEM1B bound the CTP with high affinity (K_D ~15nM) and a Hill coefficient of ~4, which is indicative of cooperative binding to multiple sites (Figure 5F–H). Mutation of either R126 or C186 of FEM1B strongly reduced, and mutation of both residues ablated, association of FEM1B with the CTP. Moreover, as TPEN abolished CTP

binding to FEM1B^{R126A}, yet had no effect on the residual CTP binding by FEM1B^{C186S}, Zn^{2+} detection by C186 of FEM1B is important for the recruitment of BEX proteins. We conclude that BEX proteins engage both R126 and the Zn^{2+} binding site of FEM1B. While mutation of R126 in FEM1B promotes substrate recognition in cells, it strongly diminishes the interaction of FEM1B with BEX proteins.

BEX proteins are pseudosubstrate inhibitors of CUL2^{FEM1B}

In line with the BEX proteins being inhibitors of CUL2^{FEM1B}, expression of BEX2 or BEX3 blocked the ability of FEM1B to induce degradation of the FNIP1 reporter (Figure 6A; Figure S7A). BEX3 also stabilized the C-end rule degron that is recognized through a similar FEM1B surface (Figure S4C; Figure S5B). Both BEX3^{C108S} and a BEX3 variant lacking carboxy-terminal His residues were unable to efficiently prevent GFP^{degron} turnover (Figure 6B). As overexpression of FNIP1 did not stabilize the GFP^{degron} reporter (Figure S7B), the inhibitory effect of BEX proteins onto FNIP1 degradation was unlikely to be caused by mere competition for access to their shared binding site on FEM1B.

Complementing our overexpression studies, depletion of BEX3 was sufficient to improve GFP^{degron} degradation through endogenous or co-expressed FEM1B (Figure 6C, D; Figure S7C), to an extent similar to the accelerated FNIP1 degradation during reductive stress (Manford et al., 2020). The increased turnover of GFP^{degron} in cells lacking BEX3 was dependent on the degron Cys residues (Figure 6D). Similar observations were made for complex formation:induction of BEX2, BEX3, or BEX4 inhibited the recognition of FNIP1 by FEM1B (Figure 5B; Figure 6E), yet BEX3^{C108S} or BEX3$^{4H/A}$ had little effect onto FNIP1-FEM1B complex formation (Figure 5E). Interestingly, while BEX1 did not prevent FNIP1 detection by FEM1B, its CTP fused to the rest of BEX3 was sufficient to block FNIP1 recognition (Figure 6E). The CTP of BEX proteins is therefore a conserved motif that is required, but not sufficient, for CUL2^{FEM1B} inhibition.

Also *in vitro*, recombinant BEX2 efficiently prevented recognition of the FNIP1 degron by FEM1B (Figure 6F, G). BEX2 accordingly blocked FNIP1 ubiquitylation by recombinant CUL2^{FEM1B}, while BEX2 itself was not significantly ubiquitylated under these conditions (Figure 6H). Together, these experiments revealed that the BEX proteins occupy the substrate binding pocket of FEM1B and inhibit FNIP1 ubiquitylation without being efficiently modified themselves. We conclude that the BEX proteins are pseudosubstrate inhibitors of CUL2^{FEM1B}.

FEM1B mutants are resistant to inhibition by BEX proteins

As FEM1B^{R126Q} did not bind BEX proteins in cells, we speculated that the pathological variant is resistant to pseudosubstrate inhibition. This hypothesis would be consistent with mutation of R126 of FEM1B and deletion of *BEX* genes eliciting similar developmental syndromes (Hijazi et al., 2020; Lecoquierre et al., 2019). Indeed, in contrast to wildtype FEM1B, mutant FEM1B^{R126Q} or FEM1B^{R126A} could still trigger GFP^{degron} degradation in the presence of BEX proteins (Figure 6A; Figure S7A). While BEX3 expression prevented binding of FEM1B to FNIP1 in cells, FEM1B^{R126Q} and FEM1B^{R126A} mutants still associated with FNIP1 under these conditions (Figure 5C; Figure S6B). *In vitro*,

FEM1B^{R126A} retained its ability to detect the FNIP1 degron in the presence of BEX2, (Figure 6F, G), and CUL2 complexes programmed with FEM1B^{R126A} continued to ubiquitylate the FNIP1 degron despite the presence of BEX2 (Figure 6H). R126 mutants of FEM1B are therefore impaired in their regulation by BEX proteins, which could account for their gain of function phenotype in disease.

BEX proteins regulate ROS production through FEM1B

Having identified BEX proteins as regulators of CUL2^{FEM1B}, we wished to assess their contribution to ROS management. Following our initial work on reductive stress signaling (Manford et al., 2020), we first investigated BEX proteins in myoblasts. In this cell type, loss of FEM1B stabilizes FNIP1 and reduces mitochondrial ROS production, yet it also leads to nuclear exclusion of the NRF2 transcription factor (Manford et al., 2020). Mirroring the consequences of FEM1B depletion, overexpression of BEX3, but not the FEM1B-binding deficient mutant BEX3^{C108S}, caused re-localization of stabilized NRF2 from the nucleus to perinuclear regions (Figure 7A).

In contrast to myoblasts, 293T cells respond to FEM1B depletion by stabilizing FNIP1 without affecting NRF2. Accordingly, loss of FEM1B slightly decreased ROS levels (Figure 7B), as expected for impaired oxidative phosphorylation in a cell type that mainly uses mitochondria for anaplerotic purposes (Manford et al., 2020). The depletion of four BEX proteins, BEX1-BEX4, caused the opposite phenotype and increased ROS, indicative of stimulated oxidative phosphorylation (Figure 7B). A similar observation was made upon stable expression of FEM1B^{R126Q}, which is defective in binding to BEX proteins and caused a premature loss of endogenous FNIP1 (Figure 7C), a rise in ROS (Figure 7D), and increased oxygen consumption indicative of more active oxidative phosphorylation (Figure 7E). As FEM1B$^{R126Q/C186S/L597A}$, which neither binds BEX proteins nor ubiquitylates FNIP1, did not display these phenotypes, it is degradation of FEM1B targets that accounts for the high ROS levels and oxygen consumption in the absence of pseudosubstrate regulation. Importantly, FEM1B^{R126Q}, but not the substrate-binding deficient FEM1B$^{R126Q/C186S/L587A}$, strongly delayed proliferation of 293T cells (Figure 7F), showing that tight control of the zinc-dependent reductive stress response through the BEX proteins is critical for cellular homeostasis.

Discussion

As the key step of the reductive stress response, the E3 ligase CUL2^{FEM1B} selectively ubiquitylates the reduced FNIP1 that is generated upon persistent ROS depletion. The ensuing degradation of this mitochondrial gatekeeper activates oxidative phosphorylation and thereby allows cells to replenish their ROS and, likely, ATP supplies. This study reveals both the structural basis and regulation of this pivotal developmental signaling circuit.

Redox-sensitive substrate binding through Zn^{2+}

We found that CUL2^{FEM1B} uses two interface zinc ions to detect FNIP1 during reductive stress. Depletion of zinc or mutation of zinc-binding residues in FEM1B or FNIP1 abrogated substrate recognition and ubiquitylation by CUL2^{FEM1B}. By contrast, preventing the few

side chain interactions, such as those mediated by FNIP1's KY-finger, only impaired, but did not obliterate, FNIP1 recognition by its E3 ligase. Zinc is therefore essential to deliver FNIP1 to $CUL2^{FEM1B}$ and works in analogy to molecular glues that are increasingly used in induced protein degradation (Jevtic et al., 2021; Petzold et al., 2016; Simonetta et al., 2019). As only reduced, but not oxidized, Cys residues bind zinc (Evans et al., 2002; Schmalen et al., 2014), these findings explain how $CUL2^{FEM1B}$ specifically detects FNIP1 during times of reductive stress (Figure 7G).

It is interesting to note that the BEX proteins also use zinc for binding to FEM1B. Moreover, the oxidative stress sensor KEAP1 is a Zn^{2+}-binding protein (Dinkova-Kostova et al., 2005; McMahon et al., 2010), as is HSP33, a chaperone that is activated by oxidative stress (Ilbert et al., 2007). These findings highlight a central role of zinc in controlling eukaryotic redox stress signaling. While the role of zinc in regulating KEAP1 remains to be fully understood, concomitant oxidative and heat stress release zinc from HSP33. This triggers local unfolding of HSP33, which increases its ability to detect unfolded proteins (Ilbert et al., 2007). How zinc is loaded onto FEM1B-FNIP1 complexes, and whether its binding or release are regulated in analogy to HSP33 awaits future studies. It is an exciting possibility that zinc fluctuations affect FNIP1 stability and mitochondrial activity, a notion that could explain why excessive zinc stimulates mitochondrial ROS production (Lee, 2018).

Zinc has been known to stabilize the structure of interaction modules, such as zinc fingers or RING domains (Klug, 2010; Plechanovova et al., 2012), but it has rarely been observed at the interface of two proteins (Cunningham et al., 1990; Hopfner et al., 2002; Kim et al., 2003; Park et al., 2017; Schmalen et al., 2014). The interfaces involving zinc ions in previous structures were small compared to additional binding surfaces formed by side chains (Park et al., 2017; Schmalen et al., 2014), and loss of zinc did not abrogate these binding events *in vitro.* By contrast, zinc is the major determinant of the FEM1B-FNIP1 interaction, and recognition of FNIP1 by FEM1B is obliterated upon zinc depletion or mutation of zinc-binding residues in this E3 ligase or substrate. Rather than a single zinc, the FEM1B-FNIP1 complex also contains two metal ions that endow FEM1B with high affinity towards FNIP1. It will be interesting to see whether other redox-regulated interactions require multiple interface zinc ions, or whether the architecture of the FEM1B-FNIP1 interface is an evolutionary adaptation to requirements of reductive stress signaling.

Coordination of reductive stress signaling and the C-end rule

While genetic studies revealed FNIP1 as the essential substrate of FEM1B in myoblasts (Manford et al., 2020), FEM1B also ubiquitylates SLBP and participates in the C-end rule pathway (Dankert et al., 2017; Koren et al., 2018; Lin et al., 2018). FEM1B recognizes the C-end rule degron through a surface that overlaps with the FNIP1 binding site (Chen et al., 2021; Yan et al., 2021). However, detection of the C-end degron by FEM1B neither required C186 nor zinc. Moreover, while the C-end rule degron is recognized with a low affinity of ~6μM (Chen et al., 2021; Yan et al., 2021), FEM1B binds FNIP1 with a high affinity of ~20nM. This suggests that zinc ions afford FEM1B with high affinity towards FNIP1 and supports genetic studies that identified FNIP1 as the prime $CUL2^{FEM1B}$ target regulating oxidative phosphorylation.

The overlap in binding sites predicts that accumulation of proteins with carboxy-terminal Arg residues could impact mitochondrial activity by preventing FNIP1 degradation. Conversely, reductive stress might prevent recognition of C-end rule substrates, a notion that is likely given the ~300-fold higher affinity of FEM1B towards FNIP1. The BEX proteins could also block ubiquitylation of both reductive stress and C-end rule substrates. Consequently, induction of BEX proteins, as it occurs in stem cells (Navas-Perez et al., 2020; Schwarz et al., 2018), might not only impact reductive stress signaling, but also protein homeostasis, thus providing an intricate example of coordination between different proteolytic pathways.

Regulation of the reductive stress response

Cells use reductive stress signaling to detect a dangerous drop in ROS and in response activate oxidative phosphorylation (Manford et al., 2020). It is therefore tempting to speculate that ROS are second messengers that report on the activity of the electron transport chain, and thus, the rate of ATP synthesis rather than ATP levels. As cells need to adjust ATP production to nutrient availability, developmental inputs, or cell cycle stage, ROS levels that trigger FNIP1 degradation should vary dependent on the cellular state.

The FEM1B-FNIP1 structure allowed us to discover how this regulation can be brought about. FNIP1 occupies only half of the conserved substrate-binding pocket in FEM1B, and the disease-linked R126 of FEM1B does not engage this substrate. Accordingly, R126 of FEM1B is not required for FNIP1 ubiquitylation, but recruits the BEX proteins that are encoded on Xq22 (Navas-Perez et al., 2020). While the BEX proteins bind with high affinity to the substrate-binding groove of FEM1B, they are not efficiently ubiquitylated by $CUL2^{FEM1B}$. Rather than being $CUL2^{FEM1B}$ substrates (Tamai et al., 2020), our analyses suggest that the BEX proteins are pseudosubstrate inhibitors of the reductive stress E3 ligase.

Pseudosubstrate inhibitors can establish tight and dynamic enzyme control (Miller et al., 2006; Newton, 2018). The few pseudosubstrate inhibitors of E3 ligases that have been studied in detail show multivalent binding to the ubiquitylation enzyme and a dearth of Lys residues as potential sites for modification (Burton et al., 2011; He et al., 2013). It is, therefore, interesting to note that all BEX proteins possess at most two Lys residues close to their FEM1B-binding CTP. Moreover, our studies suggest that the BEX proteins bind FEM1B in a multivalent manner through sites centered on C186/Zn^{2+} and R126. As BEX1 does not inhibit FEM1B despite containing a functional CTP, other BEX proteins likely contain an additional binding motif for FEM1B to effectively control reductive stress signaling. As shown with EMI1, pseudosubstrate inhibitors can switch from blocking ubiquitylation to being a substrate of the same E3 ligase, allowing for quick activation of ubiquitin transfer (Cappell et al., 2018). Whether BEX proteins can be ubiquitylated by $CUL2^{FEM1B}$ or whether their regulation depends on different mechanisms are important questions for future work.

Consistent with the role of BEX proteins as inhibitors of $CUL2^{FEM1B}$, they are expressed at high levels in stem cells that should not activate much reductive stress signaling (Navas-Perez et al., 2020; Schwarz et al., 2018). BEX2 also promotes re-programming

fibroblasts into pluripotent stem cells, a process that relies on inactivation of mitochondrial ATP production (Schwarz et al., 2018). Conversely, BEX mRNA levels decrease during differentiation (Navas-Perez et al., 2020), which should allow cells to activate oxidative phosphorylation in response to small drops in ROS. BEX proteins are overexpressed in lung and renal cancer, two tumor types that are caused by mutations in *KEAP1* or *NFE2L2* that would otherwise elicit persistent FNIP1 degradation (Uhlen et al., 2017). We speculate that BEX overexpression restricts oxidative phosphorylation in cancer cells that use glycolysis for ATP production (Warburg et al., 1927). Most importantly, deletion of *BEX* genes leads to a global developmental delay and intellectual disability that is similar to the phenotypes observed in patients in R126 mutations in *FEM1B* (Hijazi et al., 2020; Lecoquierre et al., 2019). Based on these observations, we conclude that regulation of reductive stress signaling by the opposite activities of BEX proteins and $CUL2^{FEM1B}$ is critical for organismal development. We anticipate that modulating this regulatory circuit will provide opportunities to exploit mitochondrial regulation as a therapeutic approach against cancer as well as diseases of aberrant tissue homeostasis.

Limitations of the Study

This study provides insight into the redox-dependent recognition of the FNIP1 degron by FEM1B, and regulation of this event by BEX proteins. It is possible that FEM1B detects additional domains of FNIP1 or of its constitutive binding partner FLCN, which might further fine-tune reductive stress signaling.

STAR METHODS

Resource Availability

Lead Contact—Further information and requests for reagents and resources should be directed to the Lead Contact Michael Rape (mrape@berkeley.edu).

Materials Availability—All plasmids and cell lines generated in this work can be requested from the Lead Contact. All antibodies, chemicals, and most cell lines used in this study are commercially available.

Data and Code Availability—Atomic coordinates have been deposited to the Protein Data Bank under the accession code 7ROY. This paper does not report original code or additional information.

Experimental Model and Subject Details—C2C12 myoblasts (ATCC, CRL-1772, female) and HEK293TS (ATCC, CRL-3216, female) were grown in DMEM with 10% fetal bovine serum at 37°C and 5% CO2. SF9 (ATCC, CRL-1711, female) insect cell cultures were grown at 28 °C with shaking at 125rpm in ESF921 (Expression Systems) supplemented with 1% fetal bovine serum and 1% Antibiotic-Antimycotic (Thermo Fisher, 15240062). All cell stocks and SF9 cultures were obtained from the UCB Cell Culture Facility which is supported by The University of California Berkeley.

Methods Details

Purification of FEM1B-FNIP1 complex—Since the FEM1B-FNIP1 complex was disrupted by imidazole, we employed a sequential purification using glutathione and amylose resin. A pETDuet1 construct expressing His-GST-TEV-FNIP1(562-591) and MBP-TEV-FEM1B(1-377) was grown in LOBSTR *E. coli* cells (Andersen et al., 2013) at 37°C until reaching an OD_{600} of 0.6 and then induced overnight with 0.2 mM isopropyl β-d-1-thiogalactopyranoside (IPTG) at 16°C. Cell pellets were resuspended in lysis buffer (150 mM NaCl, 50 mM Tris-HCl pH 8.0, 5 mM 2-Mercaptoethanol (ßME), and 1 mM phenylmethylsulfonyl fluoride). Cells were lysed by adding egg white lysozyme (1 mg/mL final concentration) and sonication. After centrifugation for 30 mins at 36,000 xg, clarified lysate was bound to glutathione Sepharose 4B (GE Healthcare), washed (150 mM NaCl, 50 mM Tris pH 8.0, and 5 mM ßME), and eluted with glutathione (150 mM NaCl, 50 mM Tris pH 8.0, 5 mM ßME, 10 mM reduced glutathione, 0.1% Triton X-100). The eluate was then bound to amylose resin (NEB), washed (500 mM NaCl, 50 mM Tris pH 8.0, and 1 mM TCEP), and bound complex was eluted using TEV protease (UC Berkeley Macrolab) over two days at 4 °C. Free GST protein was removed by passing the eluate over glutathione resin. Glycerol was added (20% final concentration) and the protein was concentrated and injected onto a Superdex 200 column (GE Healthcare) equilibrated with 150 mM NaCl, 20 mM Tris pH 8.0, and 1 mM TCEP. Purified FEM1B-FNIP1 complex was concentrated to 20 mg/mL, aliquoted, and flash-frozen for crystallography.

Crystallization of FEM1B-FNIP1—Crystals were grown using the hanging vapour-diffusion method in 24-well plates. FEM1B-FNIP1 complex (20 mg/mL) was mixed in a 1:1 ratio with the reservoir solution containing 6% isopropanol, 150 mM NaCl, and 100 mM HEPES-NaOH pH 7.5. Crystals with a tetragonal trapezohedron shape appeared within 3 days. Crystals were cryo-protected by soaking them in a solution containing the reservoir solution plus 20% (v/v) glycerol and they were then plunged into liquid nitrogen.

X-ray data collection and structure determination—Data were collected on the Stanford Synchrotron Radiation Lightsource beamline 14-1 at 100 K. Additionally, X-ray fluorescence spectra were obtained by excitation at the Se-K edge (12658 eV). Data collection and refinement statistics are presented in Table S1.

Data were indexed and integrated with XDS (Kabsch, 2010), then merged, scaled, and converted to structure factors using Aimless (Evans and Murshudov, 2013), Pointless (Evans, 2011), and Ctruncate (Evans, 2011). The unit cell was the space group I422 with dimensions 164.42, 164.42, and 465.21 Å. The structure was solved by the single wavelength anomalous dispersion (SAD) method using two combined 360° datasets collected at the Zn^{2+} anomalous peak wavelength (1.28227 Å). We used the Crank 2 pipeline (Skubak and Pannu, 2013) within CCP4 (Winn et al., 2011) – which employs SHELX (Uson and Sheldrick, 2018), MAPRO, Solomon (Abrahams and Leslie, 1996), Multicomb (Skubak et al., 2010), PARROT (Cowtan, 2010), BUCCANEER (Cowtan, 2006), and REFMAC (Murshudov et al., 1997) – to determine the substructure, obtain initial phases, improve them with density modification, and build the initial model. There were four copies of FEM1B in the asymmetric unit. The model was then further improved through

several iterative rounds of manual model building in COOT (Emsley et al., 2010) followed by refinement in Phenix (Adams et al., 2010) using 2.9 Å resolution data collected at a wavelength of 1.194992 Å.

Software—Crystallography analysis software was curated by SBGrid (Morin et al., 2013). UCSF Chimera (ver. 1.15, (Pettersen et al., 2004)) was used for structural analysis and generating figures. Structural alignments were performed with the Matchmaker function. For FEM1B conservation, homologs of mouse FEM1B were obtained by searching diverse phyla using NCBI blastp with the default search parameters. Homologs were considered if they were the top hit for a particular species and contained >30% sequence identity. Conservation was plotted onto the surface of FEM1B based on an alignment of 12 metazoan FEM1B homologs according to a red-white-blue color scheme. X-ray fluorescence data were plotted in R (ver. 4.0.2). Chemical stick diagrams were generated in Chemdraw (ver. 19.1).

Proteins for biochemical analyses—Full length MBP-FEM1B mutants and HIS-SUMO-BEX2 were purified as previously described (Manford et al., 2020). Briefly, mouse MBP-HIS-FEM1B (pMAL, New England Biolabs), MBP-HIS-FEM1B/Elongin B/Elongin C^{17-112} complex (pRSFduet-1, Sigma-Aldrich, 71341), and HIS-SUMO-TEV-BEX2 (pET28A) were expressed in *E.coli* LOBSTR cells grown to OD_{600} of 0.5 and then induced overnight with 0.33 mM isopropyl β- d-1-thiogalactopyranoside (IPTG) at 16°C. Cells were resuspened in lysis buffer A (50mM HEPES 7.5, 50mM NaCL, 1mM PMSF, 1mM EDTA, 5mg/ml Lysozyme) and rocked at 15 minutes at room temperature. Cell suspensions were added to ½ the volume of buffer B (50mM HEPES 7.5, 300mM NaCl 1.5mM PMSF, 15mM β-mercaptoethanol 30mM Imidazole) and cooled to 4°C. Cells were lysed by sonication and lysates cleared by centrifuging for 30,000g for 1h. The supernatant was added to washed Ni-NTA beads for 1-2 hours. Ni-NTA were washed three times for 15min with rocking in wash buffer (50mM HEPES 7.5, 150mM NaCl, 5mM β-mercaptoethanol, 20mM imidazole, and 1mM PMSF). Bound proteins were eluted with 50mM HEPES 7.5, 150mM NaCl, 5mM β-mercaptoethanol, 250mM imidazole. Elutions were dialyzed overnight in 50mM HEPES 7.5, 150mM NaCl, 5mM β-mercaptoethanol and the next day run on a HiLoad 16/600 Superdex 200pg (For FEM1B proteins) and HiLoad 16/60 Superdex 75pg (For BEX2). Protein fractions were collected, concentrated, and flash frozen. For the Tris vs HEPES fluorescence polarization assay, aliquots of HEPES purified MBP-FEM1B was desalted into either Tris (50mM Tris pH7.5, 150mM NaCl, 5mM β-mercaptoethanol) or HEPES (50mM HEPES pH7.5, 150mM NaCl, 5mM β-mercaptoethanol) containing buffers using PD midiTrap G-25 desalting columns (Cytiva, 28918008).

For $CUL2^{FEM1B}$ complex purification HIS-CUL2/RBX1 was generated from insect cells using pFastBac Dual vector. Baculovirus packaging and amplification were performed as described (Bac-to-Bac Baculovirus Expression System, Thermo Fisher). 3L of SF9 cells were infected and collected after 72 hours. Cells were lysed in 50mM HEPES 7.5, 150mM NaCl 1mM PMSF, 5mM β-mercaptoethanol, 10mM Imidazole, and 0.5% NP40 with gentle rocking at 4°C for 1h and purified as described above for MBP-HIS-FEM1B. To form CUL2-FEM1B complexes, elutions of HIS-CUL2/RBX1 and MBP-HIS-FEM1B/Elongin

B/Elongin C^{17-112} first purified as above with Ni-NTA, were mixed and added to equal volumes of 50mM HEPES 7.5, 150mM NaCl, 5mM β-mercaptoethanol, 20% glycerol. The mixture was rocked for 2 hours at 4°C and afterward 1μg/50μg TEV to protein was added to cleave the MBP and HIS tags off of FEM1B and CUL2 respectively. The TEV cleavage was performed while dialyzing overnight in 50mM HEPES 7.5, 150mM NaCl, 5mM β-mercaptoethanol, 10% glycerol. The next day complexes were separated on a HiLoad 16/600 Superdex 200pg. Complex fractions were collected, concentrated, aliquoted, and flash frozen. E1/UBA1 and UBE2R1 were purified previously described (Jin et al., 2012; Mena et al., 2018; Wickliffe et al., 2011). The neddylation machinery (human UBA3 (E1), UBE2M (E2), NEDD8) and ubiquitin were purchased from Boston Biochem (E-313, E2-656, UL-812, U-100H).

Fluorescence polarization assays—All fluorescence polarization assays were performed using a Perkin Elmer 2104 Envision plate reader. All FP data was calculated from the average of two technical duplicate mP values (1000*(S-G*P)/(S+G*P), S = 595s channel 2 and P = 595p channel 1, G=1.1) subtracted from peptide only wells and normalized to control. The assays were performed by mixing 12.5μl of MBP-FEM1B construct at indicated concentrations and treatments (BEX2 additions were added to the MBP-FEM1B mix), with 12.5μl of a peptide mix at a final concentration of 5-10nM with indicated treatments (all metal ion additions and chelator treatments were added to the peptide stock). Reactions with 0.5nM, 1nM, or 2nM peptide controlled against potential receptor depletion. All assays were done in binding buffer (40mM HEPES 7.5, 150mM NaCl, and 100μM TCEP) with 0.2% NP40 for FNIP1 peptides and 0.01% NP40 for the BEX3 peptide. For Figures S3D and 6G, FEM1B concentration was fixed at 100nM and all metal ions added to S3D were at 10μM final. For TPEN titration in Figure 1C, FEM1B concentration was fixed 125nM and peptide concentration at 50nM. For the Tris vs HEPES assay, Tris 7.5 was used in place of HEPES for all dilutions for indicated samples. TAMRA-labeled FNIP1 peptides (5,6-TAMRARNKSSLLFKESEETRTPNCNCKYCSHPVLG) and mutants were purchased from the Koch Institute/MIT Biopolymers lab. The BEX3 TAMRA-labeled peptide (5,6-TAMRARELQLRNCLRILMGELSNHHDHHDEFCLMP) was purchased from Biomatik. All graphs were generated using GraphPad Prism (GraphPad Software, Inc) using the specific binding fit with Hill slope equation. Accounting for protein depletion was not sufficient for fitting the data and fitting with a Hill coefficient improved the fit. For TPEN or BEX2 titrations, inhibitor concentration vs. normalized response with variable slope was used. Apparent K_D and apparent Hill slope are shown in Table S2.

***In vitro* ubiquitylation assays—**CUL2-ELONGIN B/C-RBX1-$FEM1B^{WT\ or\ R126A}$ complexes were neddylated in 20μl reactions with 5μM ligase complex, 6.3μM Nedd8, 500nM UBA3 (E1) and 400nM Ube2m (E2), 20mM ATP, 1mM DTT in UBA buffer (50mM Tris-HCl pH 7.5, 50mM NaCl, 10mM $MgCl_2$) at 30°C for 15min with gently shaking. For the ubiquitylation reactions Nedd8 modified $CUL2^{FEM1B}$ ligases (2μM final) were first incubated with HIS-SUMO-BEX2 (4μM final) or buffer for 5min with gently shaking at 30°C. Reactions were initiated by the addition of ubiquitylation mix consisting of 500nM TAMRA-Fnip $1^{562-591}$, 100μM ubiquitin, 20mM ATP, 0.1mM DTT, 1μM E1, 2μM UBE2R1 in UBA buffer (final volume 10μl). Reactions were incubated at 30°C for 1 hour and stopped

with 20μl 2x urea sample buffer (150mM Tris 6.5, 6M urea, 6% SDS, 25% glycerol and bromophenol blue). Reactions were analyzed by SDS-PAGE with fluorescence detection using a Protein Simple FluorChem system and immunoblot for indicated proteins. Inputs represent 100% of protein in reaction.

In vitro binding assays and co-immunoprecipitations—Binding experiments were done at room temperature in 300μl of buffer (20mM Tris 7.5, 150mM NaCl, 0.2% NP40 substitute, 100μM of TCEP, and 100 μM 1,10-Phenanthroline where indicated) with 500nM final concentration of $^{MBP\text{-}HIS}$FEM1B or ^{MBP}EPS8 and $^{HIS\text{-}SUMO}$BEX2. Binding reactions were mixed for 30 minute and then added to 20μl of Amylose bead slurry and left to bind for an addition 30 minutes. Beads were washed 4x in 1ml binding buffer and proteins eluted in 2x urea sample buffer and analyzed by SDS-PAGE. All inputs are of total protein.

For co-immunoprecipitation. 1.5 million HEK293T cells were seeded into 10cm dishes and the next day were transfected with indicated constructs. 36-40 hours' post transfection cells were harvested in phospho buffered saline (PBS) by scraping, spun down, and flash frozen in liquid nitrogen. Frozen cell pellets were resuspended in 500μl of lysis buffer (40mM HEPES 7.5, 150mM NaCl, 0.2% NP40 substitute, and cOmplete, EDTA-free protease inhibitor cocktail tablets (Sigma Aldrich, 11873580001)). For endogenous 3xFLAG-FEM1B co-immunoprecipitations, 2 15 cm plates of either HEK293TS or 3xFLAG-FEM1B C9 HEK293TS were harvested for each IP and lysed in 1200μl of lysis buffer. Lysates were gently nutated for 30 minutes at 4°C. Cell lysates were cleared with a 21,000g spin at 4°C for 30 minutes and samples normalized to protein concentration and volume using either Pierce 660nm Protein Assay Reagent (Thermo Fisher, 22660) or Abs280. Lysates were added to 20μl of prewashed ANTI-FLAG® M2 Affinity Agarose Gel slurry (Sigma-Aldrich, A2220). Beads were rocked at 4°C for 90min, spun down and washed 3x in lysis buffer without protease inhibitor. All liquid was removed before the first and last washed with a compressed gel loading tip, and proteins were eluted in urea sample buffer. Samples were analyzed by immunoblot with indicated antibodies. All inputs represent 5% of the loaded immunoprecipitated sample. For TPEN treatment, 3.5μM TPEN (Sigma-Aldrich, P4413) was added for 16 hours before harvesting the cells.

NRF2 localization with KEAP1 depletion and BEX3 overexpression—C2C12s were trypsinized and spun at 90 x g. 50k cells were resuspended in 20 μl buffer SE (Lonza V4XC-1032). Corresponding plasmid DNA constructs (1 μg) and corresponding siRNA (20 nM final in 1ml) were added to cells suspensions and gently transferred to a nucleofection strip. The samples were pulsed with program CD-137 (Lonza 4D-Nucleofector). After pulsing, cells suspensions were allowed to recover for 10 minutes and subsequently resuspended in 80 μl of pre-warmed Opti-MEM. Cell suspensions were equally divided into two wells of a 12-well plate containing borosilicate cover slips and pre-warmed growth media. Cells were fixed in 4% formaldehyde in PBS for 15min, permeabilized with 0.1% triton, and stained for NRF2 in 10% fetal bovine serum in PBS for 3 hours. Cover slips were washed and incubated for 1 hour for secondary antibody and Hoechst (AnaSpec, 83218), washed again, and mounted onto slides. Imaging was performed on an Olympus IX81 microscope equipped with a Yokogawa CSU-1X confocal scanner unit (CSUX1 Borealis

Square Upgrade Module), an Andor iXon3 camera (IXON DU-897-BV), and an Andor Technology Laser Combiner System 500 series equipped with four laser lines. Images were analyzed using Metamorph Advanced (Molecular Devices) and Fiji (Schindelin et al., 2012). NRF2 nuclear localization ratio was measured by creating a mask for the nuclei channel (Hoechst) and for the cytoplasm 1μm around the nuclei mask, the NRF2 signal from these masks was measured.

Antibodies—The following antibodies were used in this study: anti-FLAG (Clone M2, Sigma-Aldrich, F1804), anti-CUL2 (Bethyl, A302-476A), anti-FNIP1 (Abcam, ab134969), anti-FEM1B (Proteintech, 19544-1-AP), anti-beta-ACTIN (MP Biomedicals, clone C4, 691001), α-TOMM20 (Sigma-Aldrich, HPA011562), BEX2 Antibody (C-12, Santa Cruz Biotechnology, sc-398486) anti-HA-Tag (C29F4, Cell Signaling Technology (CST), 3724), anti-FLAG DYKDDDDK Tag (CST, 2368), and anti-NRF2 (D1Z9C, CST, 12721). For the endogenous 3xFLAG-FEM1B immunoprecipation, as BEX2 runs close to the antibody light chain, we used Peroxidase AffiniPure Goat Anti-Mouse IgG, Fcγ fragment specific (Jackson ImmunoResearch Laboratories, 115-035-008)

FEM1B mutant proliferation assays—To analyze the proliferation of cells expressing variants of FEM1B, HEK293Ts were infected with pLVX-^{3xFLAG}FEM1B-IRES-PURO constructs and selected for 2 days in 1μg/ml puromycin. Cells were counted and plated in 6 well plates at 150,000 cells/well. Cells were grown in the presence of 1μg/ml puromycin for the duration of the experiment. At day 3 and day 5 cells were counted using Corning Cytosmart cell counter.

Whole cell lysate—For whole cell lysates, cells were seeded into 6 well plates and media changed 12 hours prior to harvesting. Cells were washed in cold PBS and incubated in the plate with lysis buffer (1% Triton X-100, 10mM β-glycerol phosphate, 10 mM sodium pyrophosphate, 4mM EDTA, 40 mM HEPES, pH 7.4 with Roche cOmplete Protease Inhibitor Cocktail) with rocking for 10min at 4°C. Cells were scraped and transferred to tubes and rocked addition 20min at 4°C. Lysates were spun at 21,000gs for 10min at 4°C. Supernatants were collected, normalized with Pierce 660nm, and added to an equal volume of 2x urea sample buffer. Samples were heated to 65°C for 10min and analyzed by immunoblot with indicated antibodies.

Cloning—All FEM1B mutants were generated using the quick-change method and validated by sequencing. Mouse FNIP1$^{562-591}$ and FEM1B$^{1-377}$ were cloned into pETDuet1 for coexpression and purification. FNIP1 Degron mutants and CDK5R1 C-terminal degron were inserted into the pCS2+ GFP-IRES-mCherry reporter (Manford et al., 2020) by designing oligos of the degron sequences (FNIP1$^{562-591}$, CDK5R1$^{283-307}$) with indicated mutations and with the forward oligo including a 5’ CAGC and a reverse oligo a 5’ ATCA. Degron oligos were phosphorylated, annealed and ligated into the reporter construct containing the complementary overhands produced by cutting with Esp3I (New England BioLabs, R0734). All BEX genes were cloned from HEK293T cDNA and cloned into pCS2+ with N-terminal HA tags and BEX2 was also cloned into pET28A-HIS-SUMO-TEV.

ROS measurements—293T cells were split into 12 wells at 75,000 cells per well. The next day cells were transfected with indicated siRNAs and grown for an additional 48 hours. For pLVX-^{3xFLAG}FEM1B-IRES-PURO ROS measurements, selected cells were seeded 75,000 and 150,000 (For R126Q) into 12 wells. Cells were grown for 48 hours and had their media replaced. The following day ROS levels were measured. H2O2 was measured from growth media using the ROS-Glo H2O2 Assay (Promega, G8820) according the manufactures protocol. Luminescence was measured with a Perkin-Elmer Envision Multilabel Plate Reader and normalized to cell count.

Oxygen consumption measurements—HEK293T cells were infected with indicated pLVX-FEM1B-IRES-PURO viruses and selected for 1 day in puromycin as described in transfections and lentiviral packaging section. Cells were counted and plated into two 96 well black clear bottom plates at 100,000 cells per well (R126Q was seed 20% higher to compensate for proliferation defect) in 200μl of DMEM 10% Fetal Bovine Serum. The next day the media was changed 3x with a final volume 90μl, the cells were incubated for 10min at 37°C and 10μl of prewarmed MitoXpress Xtra reagent (MX-200-4, Agilent) was added to each well. Mineral oil was quickly applied to all analysis wells and samples were measured over time using Perkin Elmer 2104 Envision plate reader at 37°C using time-resolved fluorescence measurement. 6 wells for each condition were analyzed (occasional wells with negative slopes were omitted) per experiment and the average rate (RFU/hour) was normalized to cell count of three wells for each condition from the second 96 well plate (treated in a similar manner with 3 PBS washes).

Mass spectrometry—For FEM1B mutant mass spectrometry experiments 10 15cm plates were seeded with 3.5 million HEK293T cells and 24 hours later transfected with indicated FEM1B mutants. 36-40 hours post transfection cells were harvested by scraping in PBS, washed 1x, and flash frozen in liquid nitrogen. For endogenous 3xFLAG-FEM1B mass spectrometry experiment, 25 15 cm plates of 3xFLAG-FEM1B HEK293T C9 (Manford et al., 2020) cells were harvested as above. Cells were lysed in 5x wt/vol lysis buffer (40mM HEPES 7.5, 150mM NaCl, 0.2% NP40 substitute, and cOmplete, EDTA-free protease inhibitor cocktail tablets (Sigma Aldrich, 11873580001) and nutated at 4°C for 60min. Lysates were spun at 21,000g for 30min and the supernatant was added to 100μl of prewashed ANTI-FLAG® M2 Affinity Agarose Gel slurry (Sigma-Aldrich, A2220). After 1-1.5 hours of nutating, the beads were spun down and transferred to a 1.7ml tubes. Beads were washed 5x with 1.4ml lysis buffer without protease inhibitors, with all the liquid being removed with a compressed gel loading tip after the first and last wash. Beads were then washed 2x in PBS with 0.2% NP40 substitute and all of the last PBS removed with a compressed gel loading tip. Proteins were eluted with 2 times with 250μl of 500μg/ml 3xFLAG peptide (Millipore Cat#F4799) in PBS with 0.2% NP40. Elutions were pooled and precipitated in 20% final concentration of trichloroacetic acid on ice overnight. Precipitations were spun at 21,000gs for 10min and washed 3x in ice cold acetone and dried. The pellets were solubilized 8M urea 100mM Tris pH 8.5, treated with TCEP and iodoacetamide, and digested for 16-20 hours with trypsin (V5111, Promega). Samples were analyzed by Multidimensional Protein Identification Technology (MudPIT) at the Vincent J. Coates Proteomics/Mass Spectrometry Laboratory at UC Berkeley. Results were

analyzed by CompPASS analysis (Huttlin et al., 2017) comparing the samples to over 70 similarly performed anti-FLAG IPs from 293T cells. The data represents the average of 2-3 biological replicates each with 1-2 technical replicates per biological replicate. Results were normalized to 4000 bait counts with a z-score cutoff of the top 90% of unique proteins with total spectral count greater than 2. Previously published and validated interactors were also included that did not meet the Z-score cutoff. For the endogenous FEM1B mass spectrometry experiment, results were normalized to 1000 bait total spectral counts and only validated interactors are presented. Relatively stoichiometry is the ratio of total spectral counts and the number of amino acids in each protein normalized to bait = 1.

Degron reporter analysis—HEK293T cells were seeded at 300k cells per well of a 6-well plate. The next day cells were transfected with indicated reporter and any additional plasmids. 24 hour post-transfection cells were trypsinized, spun down at 300g for 5min, and resuspended in DMEM 10% fetal bovine serum. Cells were analyzed on either a BD Bioscience LSR Fortessa or LSR Fortessa X20at the University of California Berkeley flow cytometer facility, and FlowJo. GFP/mCherry ratios were determined from the median GFP and mCherry values. For TPEN and Pomalidomide treatment, TPEN was added at 2.5μM for 16hours and 10μM Pomalidomide (MedChemExpress, HY-10984) for 4 hours.

Transfections and lentiviral packaging—All siRNA transfections were performed with Lipofectamine RNAiMAX (Thermo Fisher, 13778150) using 20nM final concentration of indicated siRNA according to the manufactures protocol. When transfecting multiple siRNAs, the total siRNA amount was kept constant using control siRNA. All plasmid transfections were performed with polyethyleneimine (PEI, Polysciences 23966-1). For FEM1B mutant co-immunoprecipitation transfections, 1μg of pCS2$^{+\ 3xFLAG}$FEM1B construct and 1μg of pCS2+ were transfected in 300μl Opti-MEM with 12μl of PEI (1mg/ml). For FEM1B-BEX co-immunoprecipitation transfections, 0.5-1μg of indicated pCS2-3xFLAG-FEM1B and 2-3.5μ pCS2-HA-BEX constructs were transfected with 1:6 ratio of DNA to PEI. For FEM1B mutant mass spectrometry experiments a master mix was made where each 15cm plate was transfected with equivalent of 300μl Opti-MEM, 2μg of indicated FEM1B construct, and 12μl PEI. For FEM1B mutant FNIP1 degron flow experiments, 1μg of FEM1B construct, 0.1μg of indicated pCS2-GFP-FNIP1$^{562-591}$-IRES-mCherry construct, and 0.91μg of pCS2+ were transfected in 300μl Opti-MEM with 12μl PEI. 65μl of this reaction was used to transfect one well of a 6-well plate. For FEM1B degron flow assays comparing FEM1B and R126 mutants or BEX overexpression, 0.075μg of FEM1B construct, 0.1μg of pCS2-GFP-FNIP1$^{562-591}$-IRES-mCherry reporter or pCS2-GFP-CDK5R1$^{283-307}$-IRES-mCherry, and 1.825μg of pCS2+ or indicated BEX plasmid was transfected as above.

All lentiviral constructs were generated using Stbl3 E. Coli (Thermo Fisher Scientific, C737303). 3xFLAG-FEM1B and indicated mutants were cloned into pLVX-EF1alpha-IRES-PURO (Lenti-X Expression System Takara Bio, 631253). Lentiviral pLKO.1 constructs were purchased from Sigma-Aldrich (shBEX3, TRCN0000303798). Lentiviruses were produced in HEK293T cells by co-transfection with lentiviral constructs with packaging plasmids (pMD2.5G Addgene, 12259; psPAX2 Addgene, 12260) using PEI.

The media was collected and filtered through a 0.45μm filter and concentrated with Lenti-X concentrator following the manufactures protocol (Takara, 631232). Precipitated virus pellets were resuspended in Opti-MEM, aliquoted, and frozen. For shRNA, unattached HEK293T cells were infected with indicted viruses right after passaging the cells in the presence of 8μg/μl polybrene. For pLVX-^{3xFLAG}FEM1B-IRES-PURO infections, 200,000 HEK293T cells were put in 12 well plates with lentivirus and 8μg/ml polybrene. Cells were spun for 1 hour at 1000gs at 30°C, returned to the incubator, and split into 6 well plates the next day. Infected cells were selected with 1μg/ml puromycin 24 hours after shRNA infection or 48 hours after pLVX-^{3xFLAG}FEM1B-IRES-PURO infection.

Inductively Coupled Plasma Spectroscopy—Inductively coupled plasma spectroscopy was performed on a Perkin Elmer 5300 DV with purified proteins (0.02-0.06 mg/mL) diluted in 2% HNO_3. Standard curves (0, 0.1, and 1 μg/mL) were prepared for several transition metals (Sigma, 04330-100ML), samples were measured in triplicate, and metal concentrations were determined using a linear fit from the standard curves.

Quantification and Statistical Analysis—All quantifications are presented as the means ± standard deviation (SD). Significance was determined by 2 tailed t test, ns $p>.05$, *$p \leq 0.05$; **$p \leq 0.01$; ***$p \leq 0.001$, ****$p \leq 0.0001$.

ADDITIONAL RESOURCES

This study did not generate any additional resources.

Supplementary Material

Refer to Web version on PubMed Central for supplementary material.

Acknowledgements

We thank the Rapé and Kuriyan labs for advice; Durga Kolla for the E4F1 degron reporter; Eddie Wehri and the Henry Wheeler Center for Emerging and Neglected Diseases Drug Discovery Center; the Cancer Research Laboratory Flow Cytometry Facility; the Inductively Coupled Plasma Spectroscopy Facility the Cell Culture Facility; the Vincent J. Proteomics/Mass Spectrometry Laboratory (NIH S10RR025622); and the HTS Facility (NIH S10OD021828) at UCB. We thank the staff of Stanford Synchrotron Radiation Lightsource beamlines 14-1. Use of the Stanford Synchrotron Radiation Lightsource, SLAC National Accelerator Laboratory, is supported by the U.S. Department of Energy, Office of Science, Office of Basic Energy Sciences under Contract No. DE-AC02-76SF00515. The SSRL Structural Molecular Biology Program is supported by the DOE Office of Biological and Environmental Research, and by NIGMS (P30GM133894). A.G.M. was supported by a postdoctoral fellowship, PF-15-215-01-DCC, from the American Cancer Society; F.R.P. by a Gilliam Fellowship of the Howard Hughes Medical Institute; and ELM by a National Science Foundation fellowship. JK and MR are investigators of the Howard Hughes Medical Institute.

References

Abrahams JP, and Leslie AG (1996). Methods used in the structure determination of bovine mitochondrial F1 ATPase. Acta Crystallogr D Biol Crystallogr 52, 30–42. [PubMed: 15299723]

Adams PD, Afonine PV, Bunkoczi G, Chen VB, Davis IW, Echols N, Headd JJ, Hung LW, Kapral GJ, Grosse-Kunstleve RW, et al. (2010). PHENIX: a comprehensive Python-based system for macromolecular structure solution. Acta Crystallogr D Biol Crystallogr 66, 213–221. [PubMed: 20124702]

Andersen KR, Leksa NC, and Schwartz TU (2013). Optimized E. coli expression strain LOBSTR eliminates common contaminants from His-tag purification. Proteins 81, 1857–1861. [PubMed: 23852738]

Baba M, Keller JR, Sun HW, Resch W, Kuchen S, Suh HC, Hasumi H, Hasumi Y, Kieffer-Kwon KR, Gonzalez CG, et al. (2012). The folliculin-FNIP1 pathway deleted in human Birt-Hogg-Dube syndrome is required for murine B-cell development. Blood 120, 1254–1261. [PubMed: 22709692]

Beckervordersandforth R, Ebert B, Schaffner I, Moss J, Fiebig C, Shin J, Moore DL, Ghosh L, Trinchero MF, Stockburger C, et al. (2017). Role of Mitochondrial Metabolism in the Control of Early Lineage Progression and Aging Phenotypes in Adult Hippocampal Neurogenesis. Neuron 93, 560–573 e566. [PubMed: 28111078]

Bellezza I, Giambanco I, Minelli A, and Donato R (2018). Nrf2-Keap1 signaling in oxidative and reductive stress. Biochim Biophys Acta Mol Cell Res 1865, 721–733. [PubMed: 29499228]

Best SA, and Sutherland KD (2018). "Keaping" a lid on lung cancer: the Keap1-Nrf2 pathway. Cell Cycle 17, 1696–1707. [PubMed: 30009666]

Burton JL, Xiong Y, and Solomon MJ (2011). Mechanisms of pseudosubstrate inhibition of the anaphase promoting complex by Acm1. EMBO J 30, 1818–1829. [PubMed: 21460798]

Cappell SD, Mark KG, Garbett D, Pack LR, Rape M, and Meyer T (2018). EMI1 switches from being a substrate to an inhibitor of APC/C(CDH1) to start the cell cycle. Nature 558, 313–317. [PubMed: 29875408]

Chandel NS (2015). Evolution of Mitochondria as Signaling Organelles. Cell Metab 22, 204–206. [PubMed: 26073494]

Chen X, Liao S, Makaros Y, Guo Q, Zhu Z, Krizelman R, Dahan K, Tu X, Yao X, Koren I, et al. (2021). Molecular basis for arginine C-terminal degron recognition by Cul2(FEM1) E3 ligase. Nat Chem Biol.

Corenblum MJ, Ray S, Remley QW, Long M, Harder B, Zhang DD, Barnes CA, and Madhavan L (2016). Reduced Nrf2 expression mediates the decline in neural stem cell function during a critical middle-age period. Aging Cell 15, 725–736. [PubMed: 27095375]

Cowtan K (2006). The Buccaneer software for automated model building. 1. Tracing protein chains. Acta Crystallogr D Biol Crystallogr 62, 1002–1011. [PubMed: 16929101]

Cowtan K (2010). Recent developments in classical density modification. Acta Crystallogr D Biol Crystallogr 66, 470–478. [PubMed: 20383000]

Cunningham BC, Bass S, Fuh G, and Wells JA (1990). Zinc mediation of the binding of human growth hormone to the human prolactin receptor. Science 250, 1709–1712. [PubMed: 2270485]

Dankert JF, Pagan JK, Starostina NG, Kipreos ET, and Pagano M (2017). FEM1 proteins are ancient regulators of SLBP degradation. Cell Cycle 16, 556–564. [PubMed: 28118078]

DaRosa PA, Klevit RE, and Xu W (2018). Structural basis for tankyrase-RNF146 interaction reveals noncanonical tankyrase-binding motifs. Protein Sci 27, 1057–1067. [PubMed: 29604130]

Dinkova-Kostova AT, Holtzclaw WD, Cole RN, Itoh K, Wakabayashi N, Katoh Y, Yamamoto M, and Talalay P (2002). Direct evidence that sulfhydryl groups of Keap1 are the sensors regulating induction of phase 2 enzymes that protect against carcinogens and oxidants. Proc Natl Acad Sci U S A 99, 11908–11913. [PubMed: 12193649]

Dinkova-Kostova AT, Holtzclaw WD, and Wakabayashi N (2005). Keap1, the sensor for electrophiles and oxidants that regulates the phase 2 response, is a zinc metalloprotein. Biochemistry 44, 6889–6899. [PubMed: 15865434]

Emsley P, Lohkamp B, Scott WG, and Cowtan K (2010). Features and development of Coot. Acta Crystallogr D Biol Crystallogr 66, 486–501. [PubMed: 20383002]

Evans JC, Huddler DP, Jiracek J, Castro C, Millian NS, Garrow TA, and Ludwig ML (2002). Betaine-homocysteine methyltransferase: zinc in a distorted barrel. Structure 10, 1159–1171. [PubMed: 12220488]

Evans PR (2011). An introduction to data reduction: space-group determination, scaling and intensity statistics. Acta Crystallogr D Biol Crystallogr 67, 282–292. [PubMed: 21460446]

Evans PR, and Murshudov GN (2013). How good are my data and what is the resolution? Acta Crystallogr D Biol Crystallogr 69, 1204–1214. [PubMed: 23793146]

Fischer ES, Bohm K, Lydeard JR, Yang H, Stadler MB, Cavadini S, Nagel J, Serluca F, Acker V, Lingaraju GM, et al. (2014). Structure of the DDB1-CRBN E3 ubiquitin ligase in complex with thalidomide. Nature 512, 49–53. [PubMed: 25043012]

Gores GJ, Flarsheim CE, Dawson TL, Nieminen AL, Herman B, and Lemasters JJ (1989). Swelling, reductive stress, and cell death during chemical hypoxia in hepatocytes. Am J Physiol 257, C347–354. [PubMed: 2764095]

Gorman GS, Chinnery PF, DiMauro S, Hirano M, Koga Y, McFarland R, Suomalainen A, Thorburn DR, Zeviani M, and Turnbull DM (2016). Mitochondrial diseases. Nat Rev Dis Primers 2, 16080. [PubMed: 27775730]

He J, Chao WC, Zhang Z, Yang J, Cronin N, and Barford D (2013). Insights into degron recognition by APC/C coactivators from the structure of an Acm1-Cdh1 complex. Mol Cell 50, 649–660. [PubMed: 23707760]

Hijazi H, Coelho FS, Gonzaga-Jauregui C, Bernardini L, Mar SS, Manning MA, Hanson-Kahn A, Naidu S, Srivastava S, Lee JA, et al. (2020). Xq22 deletions and correlation with distinct neurological disease traits in females: Further evidence for a contiguous gene syndrome. Hum Mutat 41, 150–168. [PubMed: 31448840]

Hopfner KP, Craig L, Moncalian G, Zinkel RA, Usui T, Owen BA, Karcher A, Henderson B, Bodmer JL, McMurray CT, et al. (2002). The Rad50 zinc-hook is a structure joining Mre11 complexes in DNA recombination and repair. Nature 418, 562–566. [PubMed: 12152085]

Huttlin EL, Bruckner RJ, Paulo JA, Cannon JR, Ting L, Baltier K, Colby G, Gebreab F, Gygi MP, Parzen H, et al. (2017). Architecture of the human interactome defines protein communities and disease networks. Nature 545, 505–509. [PubMed: 28514442]

Ilbert M, Horst J, Ahrens S, Winter J, Graf PC, Lilie H, and Jakob U (2007). The redox-switch domain of Hsp33 functions as dual stress sensor. Nat Struct Mol Biol 14, 556–563. [PubMed: 17515905]

Ito K, Hirao A, Arai F, Matsuoka S, Takubo K, Hamaguchi I, Nomiyama K, Hosokawa K, Sakurada K, Nakagata N, et al. (2004). Regulation of oxidative stress by ATM is required for self-renewal of haematopoietic stem cells. Nature 431, 997–1002. [PubMed: 15496926]

Itoh K, Wakabayashi N, Katoh Y, Ishii T, Igarashi K, Engel JD, and Yamamoto M (1999). Keap1 represses nuclear activation of antioxidant responsive elements by Nrf2 through binding to the amino-terminal Neh2 domain. Genes Dev 13, 76–86. [PubMed: 9887101]

Itoh K, Wakabayashi N, Katoh Y, Ishii T, O'Connor T, and Yamamoto M (2003). Keap1 regulates both cytoplasmic-nuclear shuttling and degradation of Nrf2 in response to electrophiles. Genes Cells 8, 379–391. [PubMed: 12653965]

Jevtic P, Haakonsen DL, and Rape M (2021). An E3 ligase guide to the galaxy of small-molecule-induced protein degradation. Cell Chem Biol.

Jin L, Pahuja KB, Wickliffe KE, Gorur A, Baumgartel C, Schekman R, and Rape M (2012). Ubiquitin-dependent regulation of COPII coat size and function. Nature 482, 495–500. [PubMed: 22358839]

Kabsch W (2010). Xds. Acta Crystallogr D Biol Crystallogr 66, 125–132. [PubMed: 20124692]

Kim PW, Sun ZY, Blacklow SC, Wagner G, and Eck MJ (2003). A zinc clasp structure tethers Lck to T cell coreceptors CD4 and CD8. Science 301, 1725–1728. [PubMed: 14500983]

Klug A (2010). The discovery of zinc fingers and their applications in gene regulation and genome manipulation. Annu Rev Biochem 79, 213–231. [PubMed: 20192761]

Kocyla A, Tran JB, and Krezel A (2021). Galvanization of Protein-Protein Interactions in a Dynamic Zinc Interactome. Trends Biochem Sci 46, 64–79. [PubMed: 32958327]

Koren I, Timms RT, Kula T, Xu Q, Li MZ, and Elledge SJ (2018). The Eukaryotic Proteome Is Shaped by E3 Ubiquitin Ligases Targeting C-Terminal Degrons. Cell 173, 1622–1635 e1614. [PubMed: 29779948]

Lecoquierre F, Duffourd Y, Vitobello A, Bruel AL, Urteaga B, Coubes C, Garret P, Nambot S, Chevarin M, Jouan T, et al. (2019). Variant recurrence in neurodevelopmental disorders: the use of publicly available genomic data identifies clinically relevant pathogenic missense variants. Genet Med 21, 2504–2511. [PubMed: 31036916]

Lee SR (2018). Critical Role of Zinc as Either an Antioxidant or a Prooxidant in Cellular Systems. Oxid Med Cell Longev 2018, 9156285. [PubMed: 29743987]

Lin HC, Yeh CW, Chen YF, Lee TT, Hsieh PY, Rusnac DV, Lin SY, Elledge SJ, Zheng N, and Yen HS (2018). C-Terminal End-Directed Protein Elimination by CRL2 Ubiquitin Ligases. Mol Cell 70, 602–613 e603. [PubMed: 29775578]

Lisowski P, Kannan P, Mlody B, and Prigione A (2018). Mitochondria and the dynamic control of stem cell homeostasis. EMBO Rep 19.

Lu D, Ventura-Holman T, Li J, McMurray RW, Subauste JS, and Maher JF (2005). Abnormal glucose homeostasis and pancreatic islet function in mice with inactivation of the Fem1b gene. Mol Cell Biol 25, 6570–6577. [PubMed: 16024793]

Lumpkin RJ, Baker RW, Leschziner AE, and Komives EA (2020). Structure and dynamics of the ASB9 CUL-RING E3 Ligase. Nat Commun 11, 2866. [PubMed: 32513959]

Manford AG, Rodriguez-Perez F, Shih KY, Shi Z, Berdan CA, Choe M, Titov DV, Nomura DK, and Rape M (2020). A Cellular Mechanism to Detect and Alleviate Reductive Stress. Cell 183, 46–61 e21. [PubMed: 32941802]

McMahon M, Lamont DJ, Beattie KA, and Hayes JD (2010). Keap1 perceives stress via three sensors for the endogenous signaling molecules nitric oxide, zinc, and alkenals. Proc Natl Acad Sci U S A 107, 18838–18843. [PubMed: 20956331]

Mena EL, Kjolby RAS, Saxton RA, Werner A, Lew BG, Boyle JM, Harland R, and Rape M (2018). Dimerization quality control ensures neuronal development and survival. Science 362.

Miller JJ, Summers MK, Hansen DV, Nachury MV, Lehman NL, Loktev A, and Jackson PK (2006). Emi1 stably binds and inhibits the anaphase-promoting complex/cyclosome as a pseudosubstrate inhibitor. Genes Dev 20, 2410–2420. [PubMed: 16921029]

Morin A, Eisenbraun B, Key J, Sanschagrin PC, Timony MA, Ottaviano M, and Sliz P (2013). Collaboration gets the most out of software. Elife 2, e01456. [PubMed: 24040512]

Murshudov GN, Vagin AA, and Dodson EJ (1997). Refinement of macromolecular structures by the maximum-likelihood method. Acta Crystallogr D Biol Crystallogr 53, 240–255. [PubMed: 15299926]

Nam Y, Sliz P, Song L, Aster JC, and Blacklow SC (2006). Structural basis for cooperativity in recruitment of MAML coactivators to Notch transcription complexes. Cell 124, 973–983. [PubMed: 16530044]

Navas-Perez E, Vicente-Garcia C, Mirra S, Burguera D, Fernandez-Castillo N, Ferran JL, Lopez-Mayorga M, Alaiz-Noya M, Suarez-Pereira I, Anton-Galindo E et al. (2020). Characterization of an eutherian gene cluster generated after transposon domestication identifies Bex3 as relevant for advanced neurological functions. Genome biology 21, 267. [PubMed: 33100228]

Newton AC (2018). Protein kinase C: perfectly balanced. Crit Rev Biochem Mol Biol 53, 208–230. [PubMed: 29513138]

Pan W, Sun K, Tang K, Xiao Q, Ma C, Yu C, and Wei Z (2018). Structural insights into ankyrin repeat-mediated recognition of the kinesin motor protein KIF21A by KANK1, a scaffold protein in focal adhesion. J Biol Chem 293, 1944–1956. [PubMed: 29217769]

Papa L, Djedaini M, and Hoffman R (2019). Mitochondrial Role in Stemness and Differentiation of Hematopoietic Stem Cells. Stem Cells Int 2019, 4067162. [PubMed: 30881461]

Park YB, Hohl M, Padjasek M, Jeong E, Jin KS, Krezel A, Petrini JH, and Cho Y (2017). Eukaryotic Rad50 functions as a rod-shaped dimer. Nat Struct Mol Biol 24, 248–257. [PubMed: 28134932]

Pettersen EF, Goddard TD, Huang CC, Couch GS, Greenblatt DM, Meng EC, and Ferrin TE (2004). UCSF Chimera--a visualization system for exploratory research and analysis. J Comput Chem 25, 1605–1612. [PubMed: 15264254]

Petzold G, Fischer ES, and Thoma NH (2016). Structural basis of lenalidomide-induced CK1alpha degradation by the CRL4(CRBN) ubiquitin ligase. Nature 532, 127–130. [PubMed: 26909574]

Plechanovova A, Jaffray EG, Tatham MH, Naismith JH, and Hay RT (2012). Structure of a RING E3 ligase and ubiquitin-loaded E2 primed for catalysis. Nature 489, 115–120. [PubMed: 22842904]

Rajasekaran NS, Connell P, Christians ES, Yan LJ, Taylor RP, Orosz A, Zhang XQ, Stevenson TJ, Peshock RM, Leopold JA, et al. (2007). Human alpha B-crystallin mutation causes oxido-reductive stress and protein aggregation cardiomyopathy in mice. Cell 130, 427–439. [PubMed: 17693254]

Rajasekaran NS, Shelar SB, Jones DP, and Hoidal JR (2020). Reductive stress impairs myogenic differentiation. Redox Biol 34, 101492. [PubMed: 32361680]

Rajasekaran NS, Varadharaj S, Khanderao GD, Davidson CJ, Kannan S, Firpo MA, Zweier JL, and Benjamin IJ (2011). Sustained activation of nuclear erythroid 2-related factor 2/antioxidant response element signaling promotes reductive stress in the human mutant protein aggregation cardiomyopathy in mice. Antioxid Redox Signal 14, 957–971. [PubMed: 21126175]

Rodriguez-Perez F, Manford AG, Pogson A, Ingersoll AJ, Martinez-Gonzalez B, and Rape M (2021). Ubiquitin-dependent remodeling of the actin cytoskeleton drives cell fusion. Dev Cell in press.

Saettini F, Poli C, Vengoechea J, Bonanomi S, Orellana JC, Fazio G, Rodriguez FH, Noguera LP, Booth CA, Jarur-Chamy V, et al. (2020). Absent B cells, agammaglobulinemia, and hypertrophic cardiomyopathy in Folliculin Interacting Protein 1 deficiency. Blood.

Schindelin J, Arganda-Carreras I, Frise E, Kaynig V, Longair M, Pietzsch T, Preibisch S, Rueden C, Saalfeld S, Schmid B, et al. (2012). Fiji: an open-source platform for biological-image analysis. Nat Methods 9, 676–682. [PubMed: 22743772]

Schmalen I, Reischl S, Wallach T, Klemz R, Grudziecki A, Prabu JR, Benda C, Kramer A, and Wolf E (2014). Interaction of circadian clock proteins CRY1 and PER2 is modulated by zinc binding and disulfide bond formation. Cell 157, 1203–1215. [PubMed: 24855952]

Schwarz BA, Cetinbas M, Clement K, Walsh RM, Cheloufi S, Gu H, Langkabel J, Kamiya A, Schorle H, Meissner A, et al. (2018). Prospective Isolation of Poised iPSC Intermediates Reveals Principles of Cellular Reprogramming. Cell stem cell 23, 289–305 e285. [PubMed: 30017590]

Sies H, Berndt C, and Jones DP (2017). Oxidative Stress. Annu Rev Biochem.

Simonetta KR, Taygerly J, Boyle K, Basham SE, Padovani C, Lou Y, Cummins TJ, Yung SL, von Soly SK, Kayser F, et al. (2019). Prospective discovery of small molecule enhancers of an E3 ligase-substrate interaction. Nat Commun 10, 1402. [PubMed: 30926793]

Skubak P, and Pannu NS (2013). Automatic protein structure solution from weak X-ray data. Nat Commun 4, 2777. [PubMed: 24231803]

Skubak P, Waterreus WJ, and Pannu NS (2010). Multivariate phase combination improves automated crystallographic model building. Acta Crystallogr D Biol Crystallogr 66, 783–788. [PubMed: 20606258]

Spinelli JB, and Haigis MC (2018). The multifaceted contributions of mitochondria to cellular metabolism. Nat Cell Biol 20, 745–754. [PubMed: 29950572]

Suda T, Takubo K, and Semenza GL (2011). Metabolic regulation of hematopoietic stem cells in the hypoxic niche. Cell stem cell 9, 298–310. [PubMed: 21982230]

Tamai K, Nakamura-Shima M, Shibuya-Takahashi R, Kanno SI, Yasui A, Mochizuki M, Iwai W, Wakui Y, Abue M, Yamamoto K, et al. (2020). BEX2 suppresses mitochondrial activity and is required for dormant cancer stem cell maintenance in intrahepatic cholangiocarcinoma. Sci Rep 10, 21592. [PubMed: 33299012]

Tan JX, and Finkel T (2020). Mitochondria as intracellular signaling platforms in health and disease. J Cell Biol 219.

Uhlen M, Zhang C, Lee S, Sjostedt E, Fagerberg L, Bidkhori G, Benfeitas R, Arif M, Liu Z, Edfors F, et al. (2017). A pathology atlas of the human cancer transcriptome. Science 357.

Uson I, and Sheldrick GM (2018). An introduction to experimental phasing of macromolecules illustrated by SHELX; new autotracing features. Acta Crystallogr D Struct Biol 74, 106–116. [PubMed: 29533236]

Verardi R, Kim JS, Ghirlando R, and Banerjee A (2017). Structural Basis for Substrate Recognition by the Ankyrin Repeat Domain of Human DHHC17 Palmitoyltransferase. Structure 25, 1337–1347 e1336. [PubMed: 28757145]

Warburg O, Wind F, and Negelein E (1927). The Metabolism of Tumors in the Body. J Gen Physiol 8, 519–530. [PubMed: 19872213]

Wickliffe KE, Lorenz S, Wemmer DE, Kuriyan J, and Rape M (2011). The mechanism of linkage-specific ubiquitin chain elongation by a single-subunit e2. Cell 144, 769–781. [PubMed: 21376237]

Wilson JJ, and Kovall RA (2006). Crystal structure of the CSL-Notch-Mastermind ternary complex bound to DNA. Cell 124, 985–996. [PubMed: 16530045]

Winn MD, Ballard CC, Cowtan KD, Dodson EJ, Emsley P, Evans PR, Keegan RM, Krissinel EB, Leslie AG, McCoy A, et al. (2011). Overview of the CCP4 suite and current developments. Acta Crystallogr D Biol Crystallogr 67, 235–242. [PubMed: 21460441]

Yan X, Wang X, Li Y, Zhou M, Li Y, Song L, Mi W, Min J, and Dong C (2021). Molecular basis for ubiquitin ligase CRL2(FEM1C)-mediated recognition of C-degron. Nat Chem Biol.

Zhang DD, Lo SC, Cross JV, Templeton DJ, and Hannink M (2004). Keap1 is a redox-regulated substrate adaptor protein for a Cul3-dependent ubiquitin ligase complex. Mol Cell Biol 24, 10941–10953. [PubMed: 15572695]

Zipper LM, and Mulcahy RT (2002). The Keap1 BTB/POZ dimerization function is required to sequester Nrf2 in cytoplasm. J Biol Chem 277, 36544–36552. [PubMed: 12145307]

Highlights

- $CUL2^{FEM1B}$ recognizes reduced FNIP1 through two interface zinc ions
- Zn^{2+} is essential for reductive stress signaling
- FNIP1 access to $CUL2^{FEM1B}$ is gated by BEX protein pseudosubstrate inhibitors
- Mutation of *FEM1B* and *BEX* deletion cause similar developmental syndromes

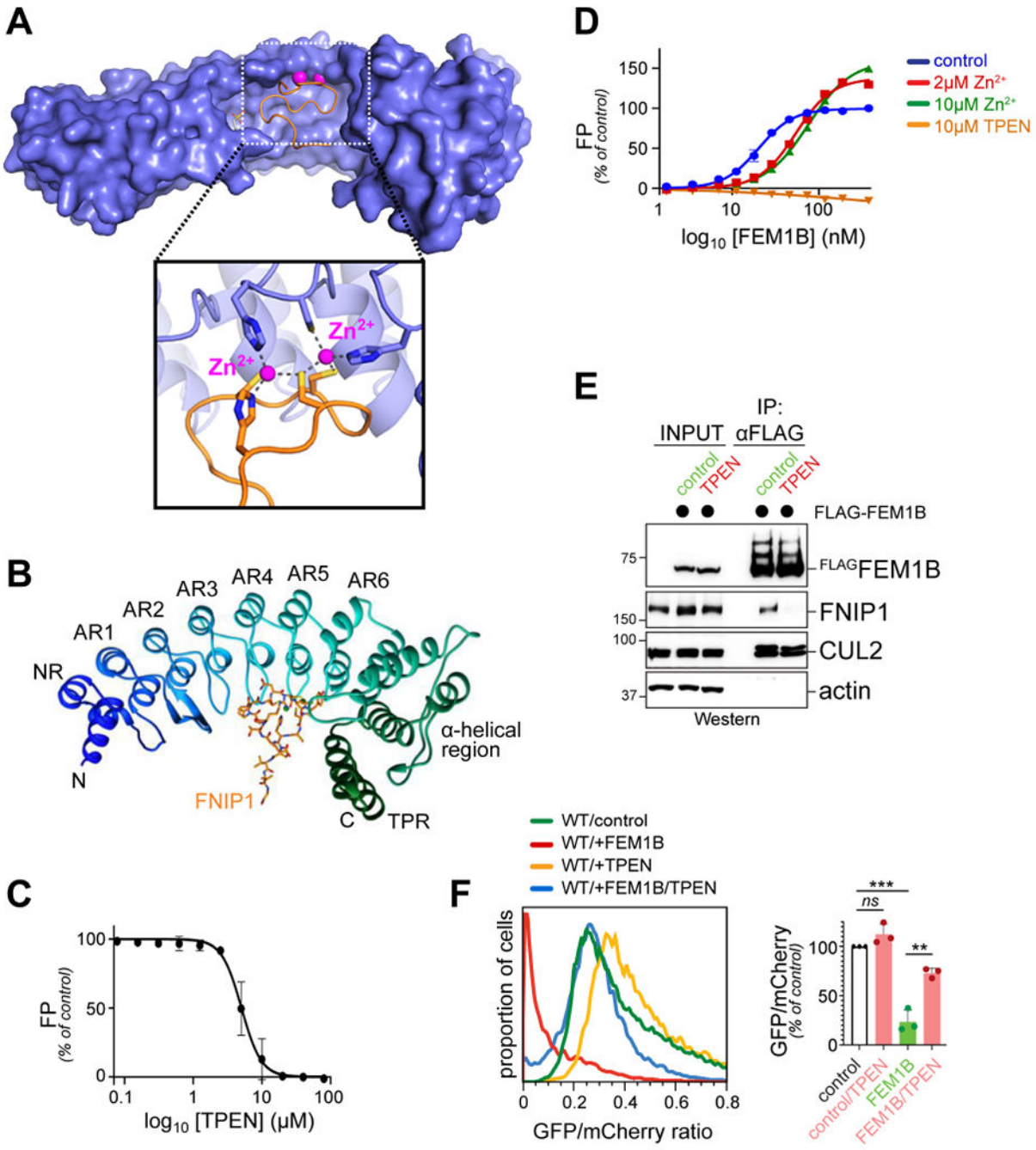

Figure 1: Interface zinc ions are essential for substrate recognition by CUL2^{FEM1B}.

A. Crystal structure of FEM1B (residues 1-377; blue) and the FNIP1 degron (residues 562-591) reveals two zinc ions (pink) at the E3-substrate interface. **B.** FEM1B contains a helical region, six ankyrin repeats, and a TPR domain that is connected through another helical region. **C.** Zinc chelation by TPEN abrogated FNIP1 recognition by FEM1B, as monitored by fluorescence polarization (FP; n=3; SD). **D.** Effects of altered zinc levels onto FNIP1 binding to FEM1B, as shown by FP. (n=3; SD). **E.** 293T cells were treated with 3.5μM TPEN, ^{FLAG}FEM1B was immunoprecipitated, and co-purifying FNIP1 or CUL2

were detected by Western blotting. **F.** Degradation of a FNIP reporter (GFP^{degron}) in relation to mCherry. TPEN treatment protected GFP^{degron} against degradation by endogenous FEM1B (green to orange shift) and exogenous FEM1B (red to blue shift). *Right panel:* quantification of median GFP/mCherry ratio (n=3; biological replicates). See also Figure S1–S3; Table S1; Table S2.

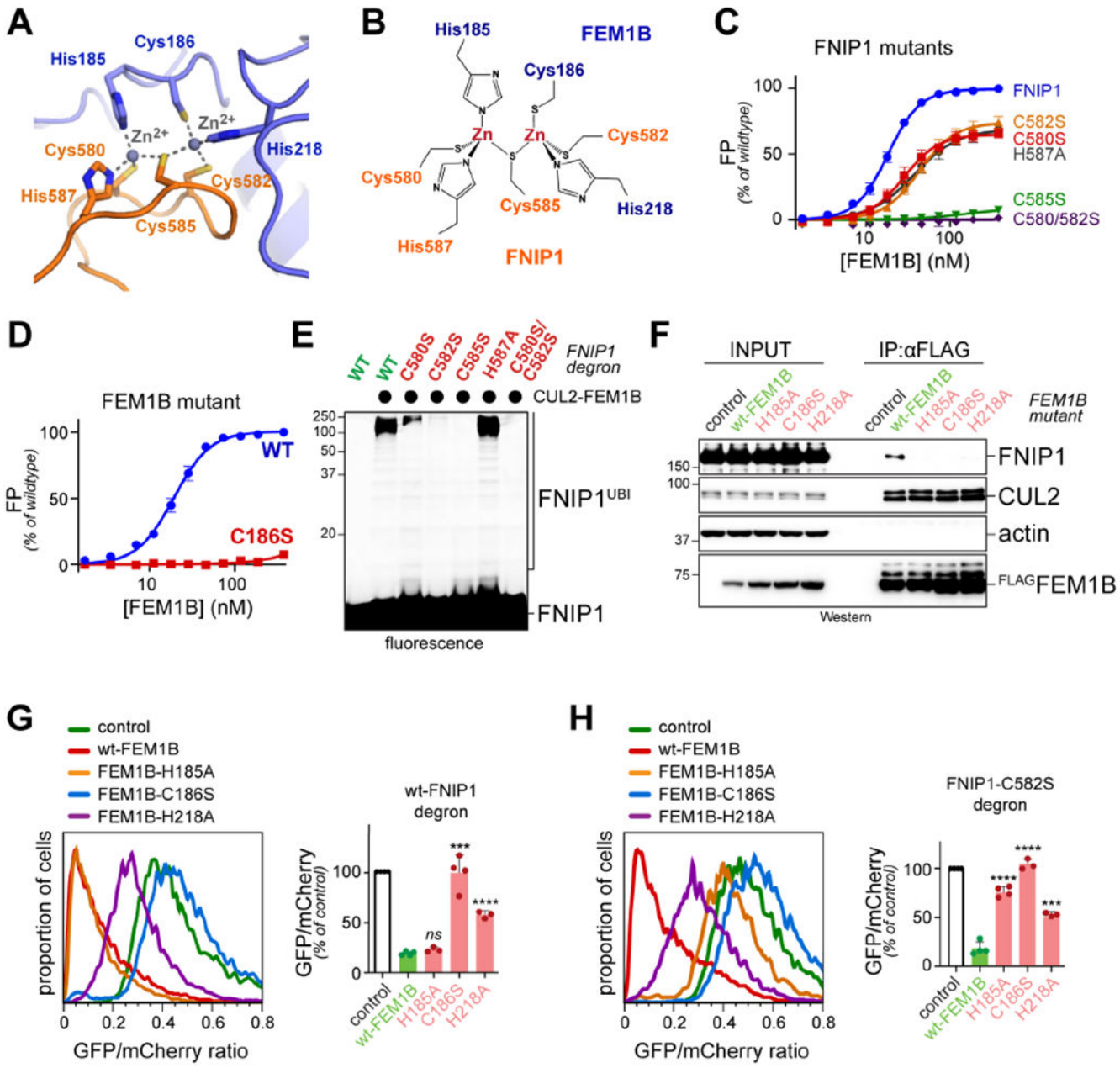

Figure 2: Zinc coordination is essential for substrate recognition by CUL2^{FEM1B}.

A. Close-up view of the interaction between FEM1B (blue) and FNIP1 (orange) shows two Zn^{2+} ions (grey) at the E3-substrate interface. **B.** Scheme of Zn^{2+} coordination by Cys and His residues of FEM1B and FNIP1. **C.** Mutation of Zn^{2+}-binding residues of FNIP1 impairs the interaction with FEM1B, as determined by FP. (n=3; SD). **D.** Mutation of C186 of FEM1B abolishes binding of a FNIP1 degron peptide. (n=3; SD). **E.** Mutation of Zn^{2+}-binding residues in the FNIP1 degron strongly impairs its ubiquitylation by recombinant Nedd8-modified CUL2^{FEM1B}. **F.** Mutation of Zn^{2+}-binding residues in ^{FLAG}FEM1B prevents recognition of endogenous FNIP1, as determined by affinity-purification and Western blotting. **G.** Mutation of Zn^{2+}-binding residues in FEM1B

protects the FNIP1 degron reporter from degradation, as determined by flow cytometry. *Right panel:* quantification of median GFP/mCherry ratio (n=3; biological replicates). **H.** Mutation of Zn^{2+}-binding FEM1B residues impairs the degradation of a GFP^{degron} carrying the C582S mutation, as determined by flow cytometry. *Right panel:* quantification of median GFP/mCherry ratio (n=3; biological replicates). See also Figure S4; Table S2.

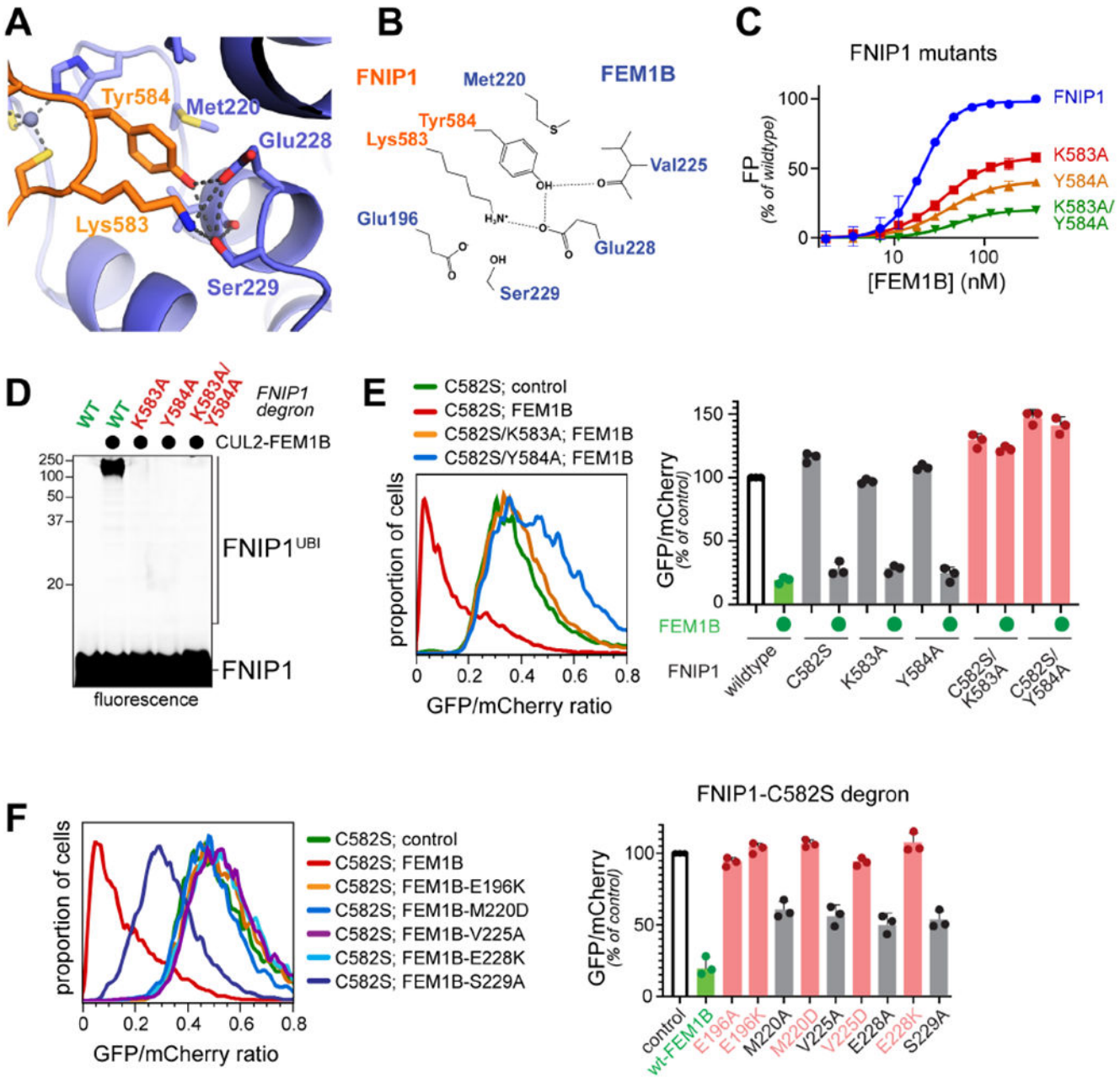

Figure 3: The KY-finger of FNIP1 orients the degron for ubiquitylation by FEM1B.

A. Close-up view of the FNIP1-FEM1B interface focused on K583 and Y584 of FNIP1. **B.** Schematic view of the FNIP1 KY-finger and its recognition by FEM1B. **C.** Mutation of K583 and/or Y584 of FNIP1 impairs binding of a FNIP1 degron to recombinant FEM1B, as determined by FP. **D.** Mutation of the KY-finger in FNIP1 strongly impairs ubiquitylation of the FNIP1 degron peptide by recombinant Nedd8-modified $CUL2^{FEM1B}$. **E.** Mutation of the KY-finger in FNIP1 prevents degradation of GFP^{degron}, when combined with mutation of C582, as determined by flow cytometry. *Right panel:* quantification of median GFP/mCherry ratio (n=3; biological replicates). **F.** Mutation of FEM1B's binding pocket for the KY-finger of FNIP1 stabilizes a sensitized GFP^{degron} reporter with the C582S mutation, as

determined by flow cytometry. *Right panel:* quantification of median GFP/mCherry ratio (n=3-4; biological replicates). See also Figure S4; Table S2.

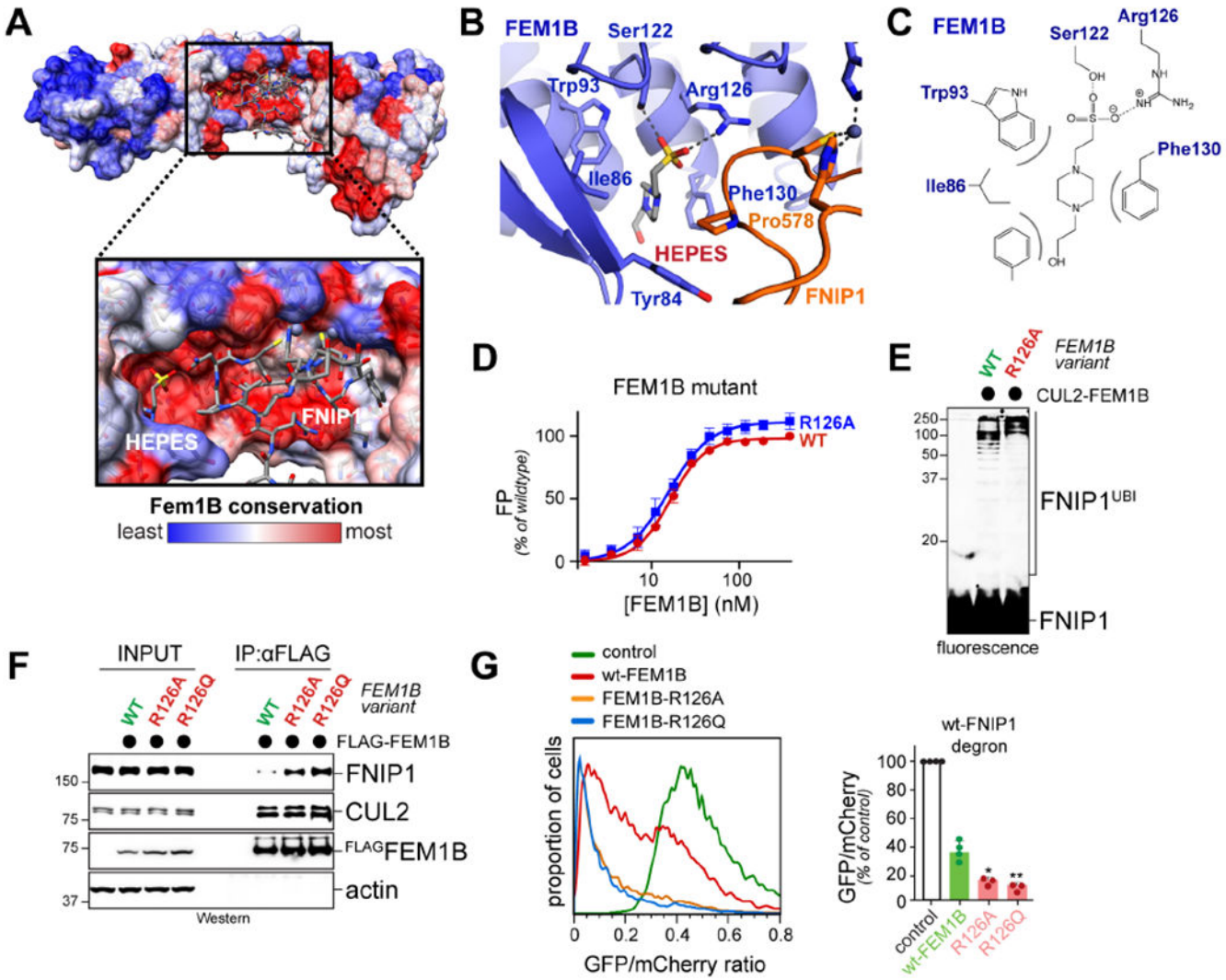

Figure 4: Disease-linked *FEM1B* mutations increase activity towards FNIP1 in cells.

A. The substrate-binding pocket of FEM1B is highly conserved. **B.** Close-up view of the FEM1B pocket bound to HEPES. **C.** Scheme of HEPES interactions with FEM1B residues. **D.** Mutation of R126 in FEM1B does not affect binding of the FNIP1 degron *in vitro*, as measured by FP. (n=3) **E.** NEDD8-modified CUL2 programmed with FEM1B^{R126A} ubiquitylates the FNIP1 degron *in vitro.* **F.** Mutants of R126 in FEM1B bind endogenous FNIP1 better than wildtype FEM1B in cells. Affinity-purified wildtype and mutant FEM1B were analyzed for co-purifying FNIP1 by Western blotting. **G.** Mutants of R126 of FEM1B target a FNIP1 reporter more efficiently for degradation, as revealed by flow cytometry. *Right panel:* quantification of median GFP/mCherry ratio (n=3-4; biological replicates). See also Figure S5; Table S2.

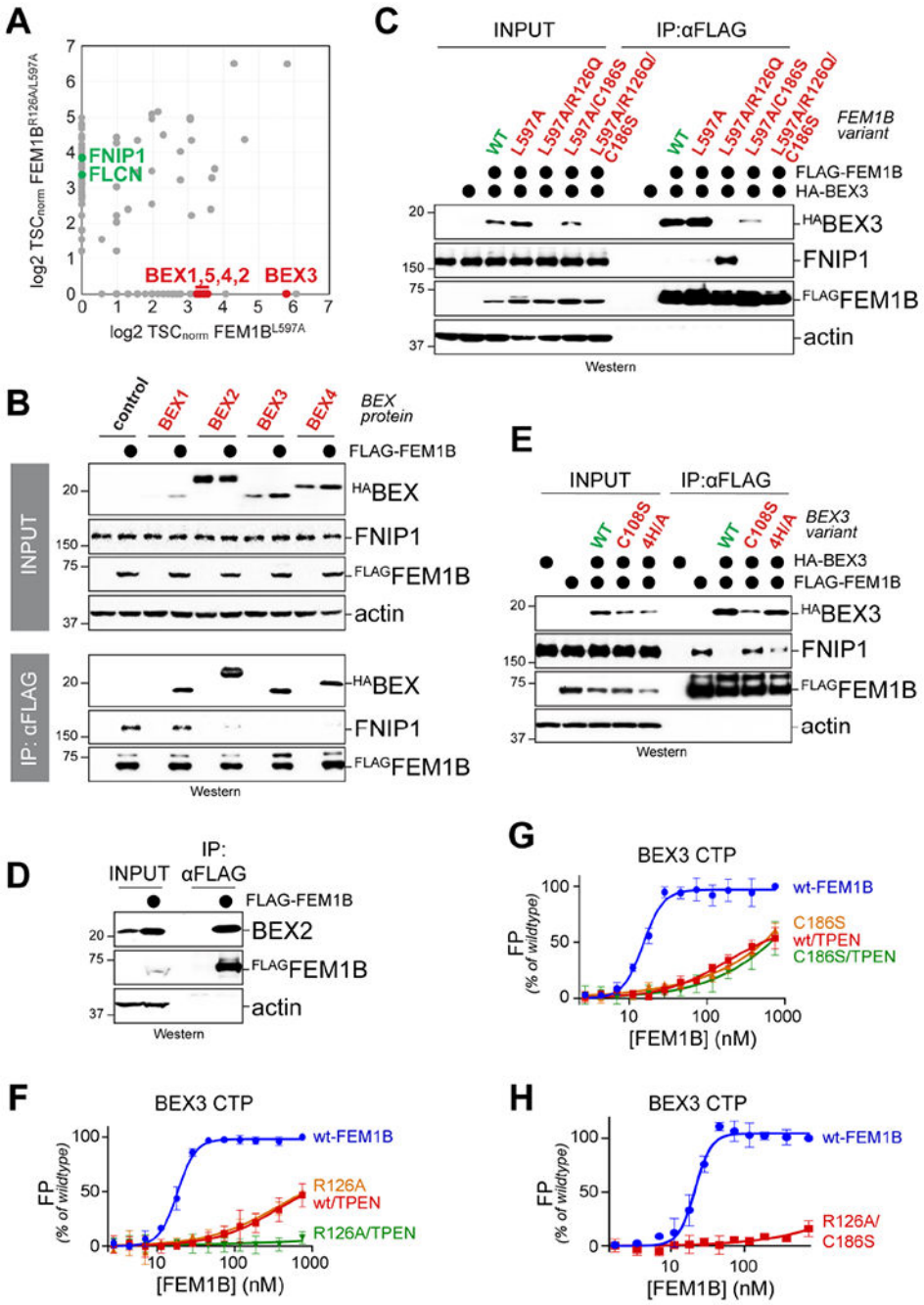

Figure 5: BEX proteins bind FEM1B dependent on R126.

A. Semi-quantitative CompPASS mass spectrometry analysis of affinity-purifications of $FEM1B^{L597A}$ and $FEM1B^{R126A/L587A}$. **B.** BEX1-BEX4 associate with FEM1B, as shown by immunoprecipitation of ^{FLAG}FEM1B and detection of co-purifying ^{HA}BEX1-4. **C.** ^{FLAG}FEM1B variants were immunoprecipitated and co-purifying ^{HA}BEX3 and endogenous FNIP1 were detected by Western blotting. **D.** Endogenous ^{FLAG}FEM1B was precipitated and co-purifying endogenous BEX2 was detected by Western blotting. **E.** Mutation of a carboxy-terminal Cys residue or a stretch of four His residues (4H/A) inhibits BEX proteins,

as shown by precipitation of ^{FLAG}FEM1B and detection of co-purifying ^{HA}BEX3 or FNIP1. **F.** Simultaneous mutation of R126 in FEM1B and zinc chelation prevents recognition of BEX3-CTP by FEM1B in FP. (n=3; SD). **G.** C186 of FEM1B is required for zinc-dependent BEX3-CTP recognition, as detected by FP. (n=3; SD). **H.** Simultaneous mutation of R126 and C186 in FEM1B prevents recognition of the BEX3-CTP by FEM1B, as monitored by FP. (n=3; SD). See also Figure S6; Table S2.

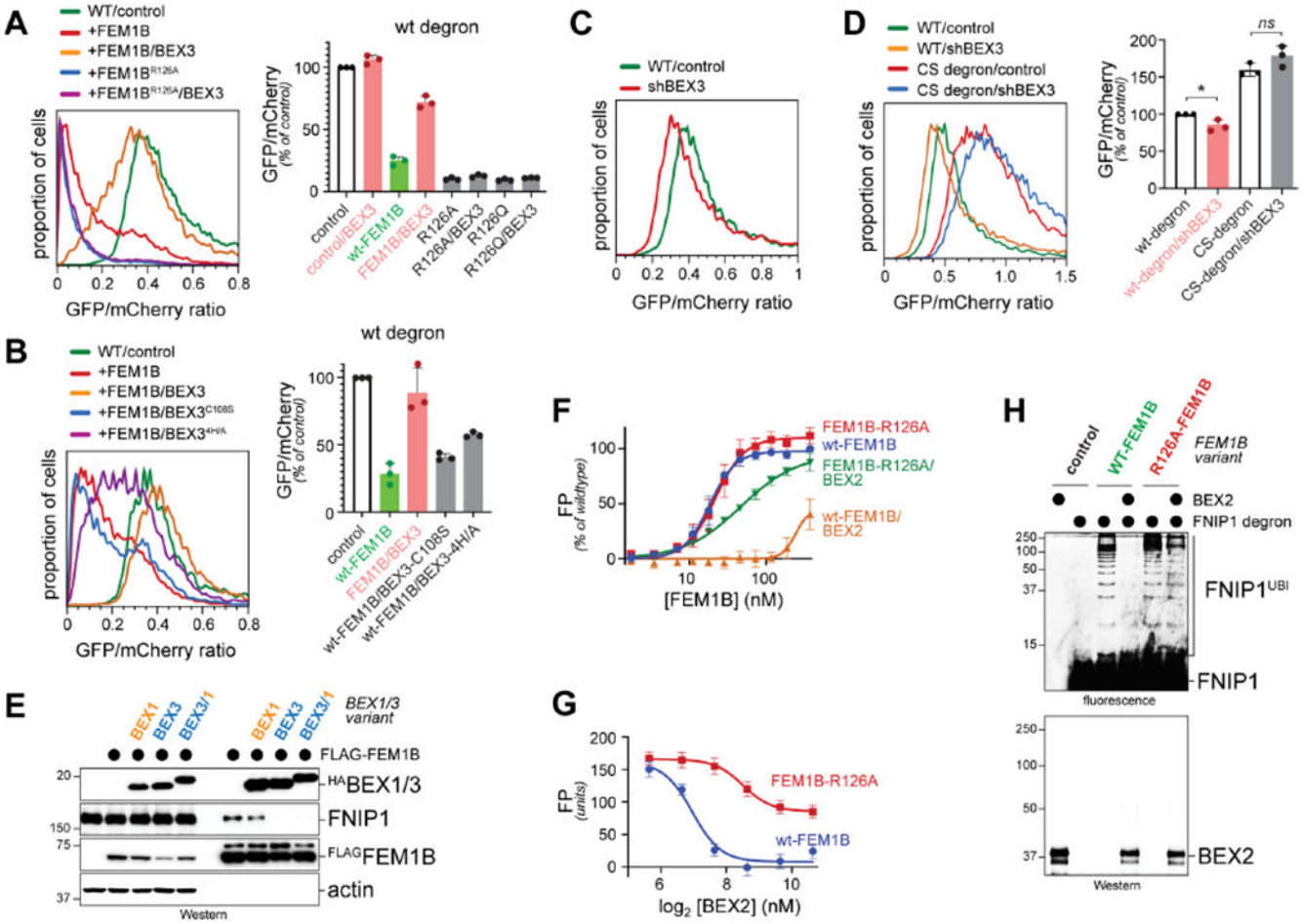

Figure 6: BEX proteins are pseudosubstrate inhibitors of CUL2^{FEM1B}.

A. BEX3 protects the FNIP1 reporter from FEM1B-, but not FEM1B^{R126A}-dependent degradation, as determined by flow cytometry. *Right panel:* quantification of median GFP/mCherry ratio (n=3; biological replicates). **B.** BEX3^{C108S} and BEX3$^{4H/A}$ are defective in preventing degradation of GFP^{degron} by FEM1B. *Right panel:* quantification of median GFP/mCherry ratio (n=4-5; biological replicates). **C.** Depletion of BEX accelerated degradation of the GFP^{degron} reporter. **D.** Accelerated degradation of GFP^{degron} upon BEX3 depletion depends on Cys residues in the FNIP1 degron, as shown by flow cytometry. *Right panel:* quantification of median GFP/mCherry ratio (n=3; biological replicates). **E.** The CTP is required, but not sufficient, to inhibit FEM1B. BEX1, BEX3 or a BEX3/1 chimera, in which the CTP of BEX3 was exchanged to that of BEX1, where assessed for their ability to prevent FNIP1 binding to FEM1B. **F.** Recombinant BEX2 prevents binding of the FNIP1 degron to FEM1B in FP. **G.** Recombinant BEX2 efficiently inhibits binding of FNIP1 to wt-FEM1B (but not FEM1B-R126A), as shown by a titration of BEX2 at constant levels of FNIP1 degron and FEM1B. **H.** Recombinant BEX2 prevents FNIP1 degron ubiquitylation by NEDD8-modified CUL2^{FEM1B}, but less by CUL2 programmed with FEM1B^{R126A}. See also Figure S6; Figure S7; Table S2.

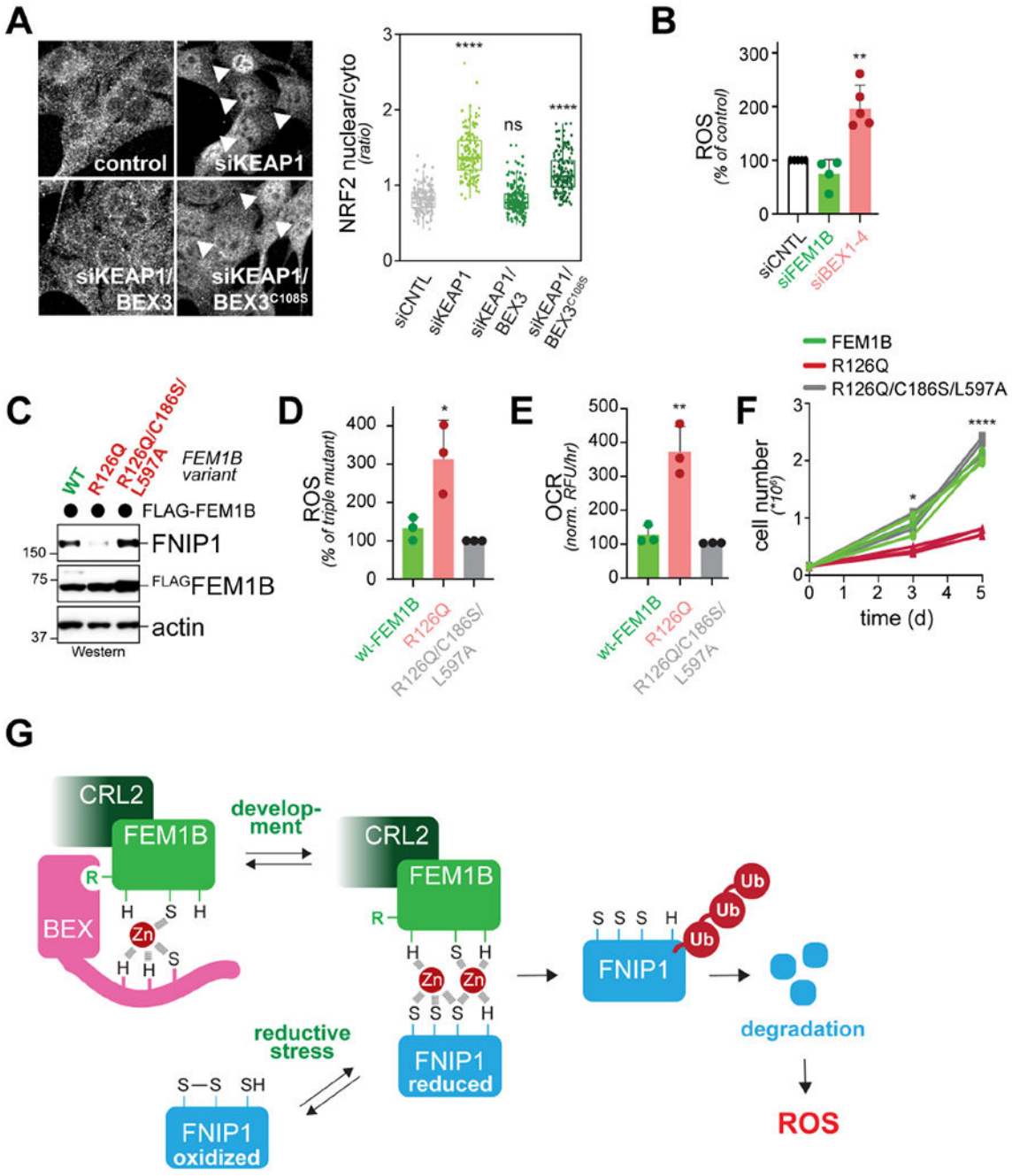

Figure 7: BEX proteins regulate ROS production in cells.

A. Overexpression of BEX3, but not BEX3^{C108S}, re-localizes myoblast NRF2, as determined by immunofluorescence microscopy. (arrow: nuclear NRF2; quantification is on the right). Scale bar 10μm. **B.** 293T cells were depleted of FEM1B or BEX1-4, and ROS levels were determined by a luciferase-based reporter. (n=3; biological replicates) **C.** Stable expression of FEM1B^{R126Q}, but not FEM1B$^{R126/C186S/L597A}$, leads to precautious degradation of endogenous FNIP1. **D.** FEM1B^{R126Q}, but not FEM1B$^{R126/C186S/L597A}$, increases ROS production. FEM1B, FEM1B^{R126Q}, or FEM1B$^{R126Q/C186S/L597A}$ were stably

expressed in 293T cells and ROS levels were monitored as above. (n=3; biological replicates) **E.** FEM1B, FEM1B^{R126Q}, or FEM1B$^{R126Q/C186S/L597A}$ were stably expressed in 293T cells and oxygen consumption rate was monitored. (n=3; biological replicates) **F.** Stable expression of FEM1B^{R126Q}, but not FEM1B$^{R126/C186S/L597A}$, strongly inhibits proliferation of 293T cells. Three independent infections and growth assays are shown for each FEM1B virus. **G.** Model of reductive stress signaling, as it is regulated by BEX proteins and Zn^{2+}-dependent binding of reduced FNIP1, to the E3 ligase CUL2^{FEM1B}.

KEY RESOURCES TABLE

REAGENT or RESOURCE	SOURCE	IDENTIFIER
Antibodies		
Mouse monoclonal anti-FLAG clone M2	Sigma-Aldrich	Cat#F1804; RRID:AB_262044
Rabbit polyclonal anti-CUL2	Bethyl	Cat#A302-476A; RRID:AB_1944215
Rabbit monoclonal anti-FNIP1 [EPNCIR107]	Abcam	Cat#ab134969
Mouse monoclonal anti-beta-ACTIN (clone C4)	MP Biomedicals	Cat#691001
Rabbit polyclonal Anti-TOMM20	Sigma-Aldrich	Cat#HPA011562; RRID:AB_1080326
Bex2 Antibody (C-12)	Santa Cruz Biotechnology	Cat# sc-398486
Rabbit monoclonal anti-HA-Tag (C29F4)	Cell Signaling Technology	Cat#3724; RRID:AB_1549585
Rabbit monoclonal anti-Flag DYKDDDDK Tag	Cell Signaling Technology	Cat#2368; RRID:AB_2217020
Rabbit monoclonal anti-NRF2 (D1Z9C XP)	Cell Signaling Technology	Cat#12721; RRID:AB_2715528
Peroxidase AffiniPure Goat Anti-Mouse IgG, Fcγ fragment specific	Jackson ImmunoResearch Laboratories	Cat#115-035-008; RRID:AB_2313585
Bacterial and Virus Strains		
E.coli LOBSTR	Laboratory of Thomas Schwartz	N/A
E.coli: One Shot Stbl3 Chemically competent cells	Thermo Fisher	Cat#C737303
Biological Samples		
Chemicals, Peptides, and Recombinant Proteins		
TAMRA-labeled FNIP1 wild type peptide (5,6-TAMRARNKSSLLFKESEETRTPNCNCKYCSHPVLG)	Koch Institute/MIT Biopolymers lab	N/A
TAMRA-labeled FNIP1 C580S peptide (5,6-TAMRARNKSSLLFKESEETRTPNSNCKYCSHPVLG)	Koch Institute/MIT Biopolymers lab	N/A
TAMRA-labeled FNIP1 C582S peptide (5,6-TAMRARNKSSLLFKESEETRTPNCNSKYCSHPVLG)	Koch Institute/MIT Biopolymers lab	N/A
TAMRA-labeled FNIP1 C585S peptide (5,6-TAMRARNKSSLLFKESEETRTPNCNCKYSSHPVLG)	Koch Institute/MIT Biopolymers lab	N/A
TAMRA-labeled FNIP1 C580/582s peptide (5,6-TAMRA-RNKSSLLFKESEETRTPNSNSKYCSHPVLG)	Koch Institute/MIT Biopolymers lab	N/A
TAMRA-labeled FNIP1 H587A peptide (5,6-TAMRA-RNKSSLLFKESEETRTPNCNCKYCSAPVLG)	Koch Institute/MIT Biopolymers lab	N/A
TAMRA-labeled FNIP1 K583A peptide (5,6-TAMRA-RNKSSLLFKESEETRTPNCNCAYCSHPVLG)	Koch Institute/MIT Biopolymers lab	N/A
TAMRA-labeled FNIP1 Y584A peptide (5,6-TAMRA-RNKSSLLFKESEETRTPNCNCKACSHPVLG)	Koch Institute/MIT Biopolymers lab	N/A
TAMRA-labeled FNIP1 K583A Y584A peptide (5,6-TAMRA-RNKSSLLFKESEETRTPNCNCAACSHPVLG)	Koch Institute/MIT Biopolymers lab	N/A
TAMRA-labeled BEX3 peptide (5,6-TAMRA-RELQLRNCLRILMGELSNHHDHHDEFCLMP)	Biomatik	N/A
$^{MBP/HIS}$FEM1B (wild-type, C186S, and R126A, and R126A C186S)	(Manford et al., 2020), this paper	N/A

REAGENT or RESOURCE	SOURCE	IDENTIFIER
^{MBP}EPS8	(Rodriguez-Perez et al., 2021)	N/A
$^{MBP/HIS}$FEM1B/ELONGIN B/ELONGIN C$^{17-112}$ complex	(Manford et al., 2020), this paper	N/A
$^{HIS-TEV}$CUL2-RBX1	(Manford et al., 2020)	N/A
CUL2^{FEM1B} (CUL2-RBX1, FEM1B wildtype or R126A/ELONGIN B/ ELONGIN C$^{17-112}$ complex)	(Manford et al., 2020), this paper	N/A
$^{HIS-SUMO-TEV}$ BEX2	this paper	N/A
E1/UBA1	Rapé lab	N/A
UBE2R1	Rapé lab	N/A
UBA3	Boston Biochem	Cat#E-313
UBE2M	Boston Biochem	Cat#E2-656
NEDD8	Boston Biochem	Cat#UL-812
UBIQUITIN	Boston Biochem	Cat#U-100H
1,10-Phenanthroline	Sigma-Aldrich	Cat#P1,280-4
Hoechst 33342	AnaSpec	Cat#83218
cOmplete, EDTA-free protease inhibitor cocktail tablets from Roche	Sigma-Aldrich	Cat#11873580001
Phenylmethanesulfonyl fluoride	Sigma-Aldrich	Cat#P7626
TPEN (N,N,N',N'-Tetrakis(2-pyridylmethyl)ethylenediamine)	Sigma-Aldrich	Cat# P4413
Transition metal mix 1 for ICP	Sigma-Aldrich	Cat# 04330-100ML
Copper(I) Chloride	Sigma-Aldrich	Cat#229628
Copper(II) Chloride	Sigma-Aldrich	Cat# 203149
Magnanese Chloride tetrahydrate	Thermo Fisher	Cat# M87-100
Magnesium Chloride hexahyrdate	Thermo Fisher	Cat# BP214-500
Calcium Chloride dihyrdrate	Sigma-Aldrich	Cat# 1.02382
Nickel 2 acetate tetrahydrate	Sigma-Aldrich	Cat# 72225
Zinc acetate dihydrate	Fluka	Cat#96459
Reduced glutathione	Sigma-Aldrich	Cat#G4251
Pomalidomide	MedChemExpress	Cat#HY-10984
Polyethylenimine (PEI), Linear, MW 25000, Transfection Grade	Polysciences	Cat#23966-1
TEV protease	UCB QB3 MacroLab	N/A
3xFLAG peptide	Millipore	Cat#F4799
TCEP (Tris(2-carboxyethyl)phosphine hydrochloride))	Sigma-Aldrich	Cat#C4706
Critical Commercial Assays		
ROS-Glo H2O2 Assay	Promega	Cat#G8820
Pierce 660nm Protein Assay Reagent	ThermoFisher	Cat#22660
MitoXpress Xtra reagent	Agilent	Cat#MX-200-4
Deposited Data		
FEM1B-FNIP1 model	This study	PDB ID 7ROY
Tankyrase-RNF146 model	(DaRosa et al., 2018)	PDB ID 6CF6

REAGENT or RESOURCE	SOURCE	IDENTIFIER
ASB9-CKB model	(Lumpkin et al., 2020)	PDB ID 6V9H
FEM1B bound to C-end rule substrate model	(Chen et al., 2021)	PDB ID 7CNG
FEM1B model without substrate	(Chen et al., 2021)	PDB ID 6LBF
Experimental Models: Cell Lines		
HEK 293T	ATCC	Cat#CRL-3216; RRID: CVCL_0063
HEK 293T 3xFLAG-FEM1B C9	(Manford et al., 2020)	
C2C12	ATCC	Cat#CRL-1772 RRID:CVCL_0188
SF9	ATCC	Cat# CRL-1711; RRID:CVCL_0549
Oligonucleotides		
ON-TARGET plus siCONT	Horizon Discovery	Cat#D-001810-03
ON-TARGET plus siFEM1B	Horizon Discovery	Cat#J-015838-06
ON-TARGET plus siBEX1 (also KD BEX2)	Horizon Discovery	Cat#J-015096-19
ON-TARGET plus siBEX3	Horizon Discovery	Cat#J-020555-07
ON-TARGET plus siBEX4	Horizon Discovery	Cat# J-024780-21
Recombinant DNA		
pCS2+ 3xFlag-FEM1B (wild-type, F81A, Y84A Y84K, W93A, S122A, S122D, R126A, R126Q, N155A, H185A, C186S,E196A, E196K, H218A, M229A, M229D, V225A, V225D, E228A, E228K, S229A, L597A, L597A/R126Q, L597A/R126A, L597A/R126Q/C186S, and L597A/R126A/C186S)	(Manford et al., 2020), this paper	N/A
pCS2+ 3xFLAG-FEM1A	(Manford et al., 2020)	N/A
pCS2+ HA-BEX1	This paper	N/A
pCS2+ HA-BEX2	This paper	N/A
pCS2+ HA-BEX3 (Wild-type, 1-96, 1-86, 1-66, H100A/H101A/H103A/H104A and C108S)	This paper	N/A
pCS2+ HA-BEX3 (1-83) - BEX1 (99-125)	This paper	N/A
pCS2+ HA-BEX4	This paper	N/A
pCS2+ FLAG-BEX3 (Wild-type and C108S)	This paper	N/A
pCS2+ HA-FNIP1	(Manford et al., 2020)	N/A
pETDuet1-HIS-GST-TEV-FNIP1(562-591) and MBP-TEV-FEM1B(1-377)	This paper	N/A
pET28A-HIS-SUMO-TEV-BEX2	This paper	N/A
pET28A-HIS-GST-TEV-FNIP1 (562-591)	This paper	N/A
pET28A-HIS-Thrombin-MBP-TEV-FEM1B (1-377)	This paper	N/A
pCS2+ E4F1 degron (220-242)-GFP-IRES-mCherry	This paper	N/A
pCS2+ GFP-CDK5R1 degron (283-307)-IRES-mCherry	This paper	N/A
pCS2+ GFP-FNIP1 degron (562-591)-IRES-mCherry (wild-type, C582S, C586, C587, C588, C589, C590, K583A, Y584A, K583A/Y584A, C582S/K583A, and C582S/Y584A)	(Manford et al., 2020), this paper	N/A
pMAL MBP-TEV2x-HIS6-FEM1B (wild type, C186S, and R126A)	(Manford et al., 2020), this paper	N/A
pRSFDuet-1 Elongin B, ElonginC^{17-112}	(Manford et al., 2020)	N/A
pFastBac Dual HIS6-TEV-CUL2, RBX1	(Manford et al., 2020)	N/A

REAGENT or RESOURCE	SOURCE	IDENTIFIER
shBEX3	Sigma-Aldrich	Cat#SHCLNG TRCN0000046535
pLVX-EF1alpha-IRES-PURO	Takara BIo	Cat#631253
pLVX-EF1alpha-3xFLAG-FEM1B-IRES-PURO (wild type, R126Q, R126Q/C186S/L597A)	This paper	N/A
Software and Algorithms		
GraphPad Prism	GraphPad Software, Inc	RRID:SCR_002798
Metamorph Advanced	Molecular Devices	RRID:SCR_002368
FlowJo	Flowjo	RRID:SCR_008520
Fiji	(Schindelin et al., 2012)	RRID:SCR_002285
Chemdraw (ver. 19.1)	PerkinElmer Informatics	RRID:SCR_016768
COOT (ver. 0.9.3)	(Emsley et al., 2010)	RRID:SCR_014222
UCSF Chimera (ver. 1.15)	(Pettersen et al., 2004)	RRID:SCR_004097
Phenix	(Adams et al., 2010)	RRID:SCR_014224
XDS	(Kabsch, 2010)	RRID:SCR_015652
Aimless	(Evans and Murshudov, 2013)	RRID:SCR_015747
Pointless	(Evans, 2011)	RRID:SCR_014218
CCP4	(Winn et al., 2011)	RRID:SCR_007255
Ctruncate	(Winn et al., 2011)	RRID:SCR_007255
SBGRID	(Morin et al., 2013)	RRID:SCR_003511
Shelx	(Uson and Sheldrick, 2018)	RRID:SCR_014220
Solomon	(Abrahams and Leslie, 1996)	N/A
Multicomb	(Skubak et al., 2010)	N/A
Parrot	(Cowtan, 2010)	N/A
Buccaneer	(Cowtan, 2006)	RRID:SCR_014221
Refmac	(Murshudov et al., 1997)	RRID:SCR_014225
CompPASS	(Huttlin et al., 2017)	N/A
Other		
Opti-MEM	Thermo Fisher	Cat#31985-070
SE Cell Line 4D-NucleofectorTM X Kit S	Lonza	Cat#V4XC-1032
Lipofectamine RNAiMAX	ThermoFisher	Cat#13778150
ANTI-FLAG® M2 Affinity Agarose Gel slurry	Sigma-Aldrich	Cat#A2220
Ni-NTA	QIAGEN	Cat#30210
HiLoad 16/60 Superdex 75pg	GE Healthcare/Cytiva	Cat#28-9893-33
HiLoad 16/600 Superdex 200pg	GE Healthcare/Cytiva	Cat#28-9893-35
Glutathione Resin	GE Healthcare/Cytiva	Cat#17075605
PD midiTrap G-25	Cytiva	Cat#28918008
LentiX concentrator	Takara	Cat#631232
Amylose Resin	New England Biolabs	Cat#E8021L